Journal of Petroleum Science and Engineering 214 (2022) 110468

Contents lists available at ScienceDirect

Journal of Petroleum Science and Engineering

journal homepage: www.elsevier.com/locate/petrol

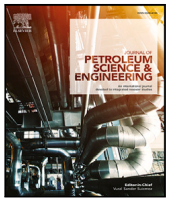

An iteratively coupled model for flow, deformation, and fracture propagation in fractured unconventional reservoirs

Harun Rashid [a], Olufemi Olorode [a,*], Chukwudi Chukwudozie [b]

[a] Louisiana State University, Baton Rouge, 70803, LA, United States
[b] Amazon, Seattle, 98109, WA, United States

ARTICLE INFO

Keywords:
pEDFM
XFEM
Coupled flow and geomechanics
Fracture propagation
Naturally fractured reservoirs
Hydraulic fracture modeling
Iterative coupling

ABSTRACT

The accurate and efficient modeling of hydraulic fracture propagation is required to design optimal hydraulic fracture jobs in fractured tight rocks. To this end, we propose and demonstrate the first fixed-stress coupling of pEDFM with XFEM to model hydraulic fracture propagation in naturally fractured reservoirs. This addresses the limitation of EDFM to low-conductivity fractures and is much faster than DFM and fully coupled schemes, which have mostly been applied to the modeling of fracture propagation in fractured reservoirs. The validation studies presented indicate the accuracy of our model at reproducing the analytical solutions to coupled geomechanics and fracture propagation problems. We show that the iterative coupling of pEDFM with XFEM accounts for the interaction between the propagating hydraulic fracture and low-conductivity natural fractures in its vicinity, whereas EDFM does not. This is important when modeling hydraulic fracturing and the subsequent production from multiply fractured hydraulic wells. The iterative coupling approach used in this work provides the flexibility and simplicity needed to model complex fluid and rock behaviors in unconventional oil and gas reservoirs.

1. Introduction

The production of oil and gas from petroleum reservoirs involves several coupled physical mechanisms, which vary in importance depending on the recovery mechanisms and reservoir rock and fluid properties. These coupled mechanisms could include fluid flow, mechanical deformation and fracturing, chemical reactions, and heat flow. When modeling primary recovery from conventional petroleum reservoirs, we mainly focus on fluid flow and ignore other physical mechanisms. However, in unconventional oil and gas (UOG) reservoirs, we typically consider additional mechanisms such as mechanical deformation and hydraulic fracture propagation. This is because of the importance of hydraulic fractures in the commercial development of these reservoirs. With the increased contribution of UOG reservoirs to the total US oil and gas production over the last decade, several researchers have focused on the modeling of hydraulic fracturing and the production from multiply fractured horizontal wells. Developing a fast and accurate model to predict hydraulic fracture propagation and the subsequent production from UOG reservoirs is essential to optimizing hydraulic fracture jobs, production constraints, and well and fracture spacing.

Hydraulic fracturing in the oil and gas industry today is still largely empirical and based on field experience. However, the current state of the art has evolved to leverage analytical and simplistic numerical tools that help make critical decisions during the fracturing job. The analytical techniques used to interpret real-time hydraulic fracturing data include the step-down rate tests, pre-closure analyses based on the G-function and square-root time analyses, and the after-closure analyses based on Nolte (1979), Nolte et al. (1997) and Soliman et al. (2005). Although these analytical techniques are fast enough to be used in real-time during hydraulic fracturing, they only give qualitative information on the fracture properties. This limits their usefulness in truly optimizing hydraulic fracturing jobs to maximize the production from hydraulically fractured UOG reservoirs. So, the oil and gas industry typically uses commercial simulators that are based on simplistic assumptions about the geometry of the propagating fractures. Some of the simplistic models implemented in these simulators include the KGD (Geertsma and De Klerk, 1969; Khristianovic and Zheltov, 1955), PKN (Perkins and Kern, 1961), planar 3D (Siebrits and Peirce, 2002), and pseudo-3D models (Dontsov and Peirce, 2015).

Although the simplifying assumptions in most commercial hydraulic fracturing simulators make them fast enough for real-time hydraulic fracturing optimization, they are typically unable to model fracture propagation in a fully 3D domain. Additionally, most of these simulators cannot rigorously model the expected interaction between the propagating fracture and individual natural fractures in these tight

* Corresponding author.
E-mail addresses: hrashid@nevada.unr.edu (H. Rashid), folorode@lsu.edu (O. Olorode), chdozie@gmail.com (C. Chukwudozie).

https://doi.org/10.1016/j.petrol.2022.110468
Received 9 November 2021; Received in revised form 11 February 2022; Accepted 22 March 2022
Available online 6 April 2022

rocks (Rahman and Rahman, 2013; Liu et al., 2014). Therefore, various researchers have developed numerical models to simulate the propagation of only a few hydraulic fractures in 3D. Most of these models are based on the finite element method (FEM) (Clifton and Abou-Sayed, 1981) and can account for the coupled flow and mechanical deformation of the reservoir and fracture propagation. However, the standard FEM does not conserve mass and fluxes at the element interfaces and requires upwinding to obtain non-oscillatory solutions. So, most finite element simulations of coupled flow and geomechanics are limited to the flow of incompressible fluids. The modeling of hydraulic fracture propagation with the standard FEM requires re-meshing the simulation domain (which conforms to the fracture geometry) as the fracture propagates (Khoei, 2014).

To ensure the conservation of mass and fluxes when solving the coupled flow and geomechanics problem, some researchers have combined the use of the finite volume method for flow with FEM (Kim, 2010; Efendiev et al., 2015). The embedded discrete fracture model (Li and Lee, 2008) was developed to efficiently account for each fracture in a reservoir without conforming the matrix mesh to the geometry of the fractures, as in the discrete fracture model (Kim and Deo, 2000; Karimi-Fard and Firoozabadi, 2001). Ţene et al. (2017) showed that EDFM does not account for low-conductivity fractures, and presented the projection-based EDFM (pEDFM) to address this limitation. Using these fracture models in finite volume simulators ensures the conservation of mass and fluxes in both matrix and fracture cells. FEM has also been extended to facilitate fracture propagation modeling (without re-meshing) by adding enrichment functions to the standard finite-element approximations. The extended finite element method (XFEM) (Moës et al., 1999; Dolbow, 1999) significantly enhances the modeling of cracks by its use of the partition of unity (PoU) to locally enrich the basis functions with a Heaviside step function for the crack surface, and an asymptotic function for the crack tip (Duarte and Oden, 1996; Melenk and Babuška, 1996). The PoU enables the definition of a set of functions that sums up to unity on a domain of interest.

The modeling of hydraulic fracture propagation in naturally fractured reservoirs is essential, considering that virtually all petroleum reservoirs are naturally fractured to some extent. This is even more important in UOG reservoirs, which are typically naturally fractured and require hydraulic fracturing for commercial development. A few authors have proposed using EDFM and XFEM to model the coupled flow, deformation, and fracturing of naturally fractured reservoirs. Ren and Younis (2020) modeled fully coupled flow and geomechanics using EDFM and XFEM, and later extended this to model fully coupled flow, geomechanics, and hydraulic fracture propagation (Ren and Younis, 2020). Wang et al. (2020) presented an algorithm that couples EDFM and XFEM, but they mentioned that their study does not account for the effect of the pore pressure on mechanical deformation.

Hydraulic fractures have been observed to easily propagate further into the matrix when the fracture length is greater than approximately one meter because the tensile strength becomes irrelevant, and stresses tend to concentrate at the fracture tips (Zoback, 2010). This leads to a dissipation of some of the energy needed to open up the fracture (mode I fracture) against the least principal stress, resulting in small fracture apertures. Smaller fractures lead to low fracture conductivity and make the modeling of such fractures with EDFM questionable. This work presents the first sequential/iterative coupling of pEDFM with XFEM, which enables the rigorous modeling of coupled flow, deformation, and hydraulic fracturing in reservoirs where the natural fractures could either be sealing or conductive.

Kim (2010) discussed four different sequential (or iterative) coupling approaches to solve the coupled flow and geomechanics problems. These include the fixed-stress, fixed-strain, drained, and undrained splitting schemes. The fixed-strain and drained splitting approaches are shown to be conditionally stable at best, while the fixed-stress and undrained splitting schemes are unconditionally stable. Furthermore, the fixed-stress splitting approach exhibits faster convergence than the undrained splitting scheme. This work extends the fixed-stress splitting coupling of the flow and geomechanics equations to account for hydraulic fracture propagation. Unlike most previous studies that use a fully coupled solution approach, this sequentially coupled approach allows us to solve the flow and mechanical problems sequentially within a loop.

One of the unique advantages of this approach includes the improved computational efficiency when modeling hydraulic fracture propagation in the presence of pre-existing fractures. This is because the solution of the flow and mechanical problems separately implies that we only need to invert two smaller matrix systems instead of inverting one large matrix system, as in the fully coupled approach. The modeling of fluid flow in fractures with pEDFM also helps improve the computational efficiency because the mesh does not have to conform to the geometry of all natural fractures as in the discrete fracture model (DFM). Another advantage of the proposed approach lies in the flexibility of combining different flow and geomechanics simulators (Bostrøm and Skomedal, 2004; Li et al., 2019), and the ability to model larger simulation domains in the mechanical problem than in the flow problem.

The rest of this paper begins with the governing equations for flow in matrix and fractures and the linear momentum balance equation for the mechanical deformation of a porous medium. These equations are then numerically discretized using the finite volume method (FVM) for fluid flow and XFEM for the linear momentum balance equation. Next, we present our extension of the fixed-stress splitting approach to model hydraulic fracture propagation and conclude the paper with a discussion of the verification and application of our simulation model.

2. Governing equations

This section presents the partial differential equations (PDE) that govern fluid flow in deformable reservoir matrices and fractures, as well as the equations that describe the deformation of fractured porous media. The constitutive relationships used in these PDEs are also provided.

2.1. Flow in a deformable porous matrix

The governing equation for single-phase flow in a deformable porous matrix can be given as (Kim, 2010):

$$\phi_m \rho_l c_l \frac{\partial p_m}{\partial t} + \rho_l \frac{\alpha - \phi_m}{K_s} \frac{\partial p_m}{\partial t} + \alpha \rho_l \frac{\partial \epsilon_v}{\partial t} + \nabla \cdot \left(\rho_l v_l\right) = \rho_l q / V_b. \tag{1}$$

Here, ρ_l is density of the fluid, ϕ_m is the true porosity of the matrix (that is, the ratio of the current pore volume to the current bulk volume), K_s represents the bulk modulus of the solid grain, c_l is the liquid compressibility, and α is the Biot coefficient. The symbol ϵ_v represents the volumetric strain of the porous medium, k_m is the matrix permeability, μ is the fluid viscosity, g represents the acceleration due to gravity, p_m is the pore pressure in the matrix, t is time, and z refers to the depth. The symbol q on the right-hand side of the equation represents the contribution from a source/sink, and is multiplied by density and divided by bulk volume (V_b) to ensure dimensional consistency. The liquid flow velocity (v_l) in Eq. (1) can be obtained from the Darcy equation, which is a constitutive equation that relates flow velocity and pressure gradient, as follows:

$$v_l = -\frac{k_m}{\mu}[\nabla p_m - \rho_l g \nabla z]. \tag{2}$$

The Biot coefficient can be written as a function of the bulk modulus of the drained rock skeleton and that of the solid grains (K_{dr} and K_s), as follows (Coussy, 2007):

$$\alpha = 1 - \frac{K_{dr}}{K_s}. \tag{3}$$

Hooke's law can be written in terms of total volumetric stress (σ_v) and volumetric strain (ϵ_v) as follows:

$$\left(\sigma_v - \sigma_{v,0}\right) + \alpha\left(p_m - p_{v,0}\right) = K_{dr}\epsilon_v, \tag{4}$$

where the zero subscripts indicate that the corresponding quantities are defined at the initial state. Differentiating each term with respect to time and multiplying through by α yields:

$$\frac{\alpha}{K_{dr}}\frac{\partial \sigma_v}{\partial t} + \frac{\alpha^2}{K_{dr}}\frac{\partial p_m}{\partial t} = \alpha\frac{\partial \epsilon_v}{\partial t}. \tag{5}$$

Substituting this into Eq. (1) yields the governing equation (for flow in a deformable porous matrix) in terms of the total volumetric stress:

$$\rho_l\left[\phi_m c_l + \frac{(\alpha-\phi_m)}{K_s} + \frac{\alpha^2}{K_{dr}}\right]\frac{\partial p_m}{\partial t} + \rho_l\frac{\alpha}{K_{dr}}\frac{\partial \sigma_v}{\partial t} - \nabla\cdot\left(\rho_l\frac{k_m}{\mu}[\nabla p_m - \rho_l g\nabla z]\right) - \rho_l q/V_b = 0. \tag{6}$$

2.2. Flow in fractures

This subsection discusses the modeling of fluid flow in fractures using either the cubic law (based on lubrication theory) for flow in parallel plates or flow in porous media, which has been used in virtually all previously published attempts of coupling EDFM or pEDFM with XFEM.

2.2.1. Use of cubic law for the fluid flow in fractures

In standard fracture propagation models that represent the fracture as a line (for 2D reservoir models), the pressures on the nodes that make up this line are applied as internal boundary conditions. The governing equation for fracture flow based on lubrication theory can be given (for a 2D system) as (Batchelor, 1967):

$$\frac{\partial w_f}{\partial t} - \frac{\partial}{\partial x}\left(\frac{w_f^3}{12\mu}\frac{\partial p_f}{\partial x}\right) + g(x) = 0, \tag{7}$$

where w_f refers to the fracture aperture, $g(x)$ refers to the leakage of the fracture fluid into the surrounding porous medium, and subscript f refers to the fracture. It is worth mentioning that this equation is referred to as the cubic law, because w_f is raised to a power of three. An estimation of the permeability from the flow through parallel plates using this equation yields the well-known equation for fracture permeability ($k_f = w_f^2/12$). Substituting this definition of k_f and integrating over a fracture domain ($\Delta x\Delta y$) yields:

$$\int_\Omega \frac{\partial w_f}{\partial t}dxdy - \int_\Omega \nabla\cdot\left(\frac{w_f k_f}{\mu}\nabla p_f\right)dxdy + \int_\Omega g(x)\,dxdy = 0 \tag{8}$$

Integrating using the Green's theorem, we obtain:

$$\frac{\Delta w_f}{\Delta t}L_f w_f - \int_{\partial\Omega}\left(\frac{w_f k_f}{\mu}\nabla p_f\right)ds + g(x)\,L_f w_f = 0 \tag{9}$$

2.2.2. Use of porous medium approach for fluid flow in fractures

The governing equation for 1D flow in non-deformable porous media is given as:

$$\phi_f c_l\frac{\partial p_f}{\partial t} - \nabla\cdot\left(\frac{k_f}{\mu}\left[\nabla p_f - \rho_l g\nabla z\right]\right) - q/V = 0, \tag{10}$$

for slightly compressible or incompressible fluids, where the fluid density is assumed constant. Even when the gravity and source/sink terms in Eq. (10) are ignored, an inspection of both equations reveals that Eq. (10) does not account for the variation of the fracture aperture in space (in the flux term) and in time (in the storage term). So, the units of each term in Eq. (10) differ from those in Eq. (7) by one length scale. Although Eq. (10) might be applicable in propped hydraulic fractures because it was developed for porous media, its applicability in open cracks without sands/proppants could be questionable. To enable the modeling of propped or unpropped hydraulic fractures, we developed a simulator that is able to use either Eq. (7) or (10). If we consider compressible fluids, the governing equation for fluid flow in the propped fractures will be similar to that for flow in the matrix, but with the assumption that the fracture is unable to support shear stresses. So, we neglect the contributions from the volumetric strain, matrix skeleton, and solid grain deformation in Eq. (6) to obtain:

$$\rho_l\phi_f c_l\frac{\partial p_f}{\partial t} - \nabla\cdot\left(\rho_l\frac{k_f}{\mu}\left[\nabla p_f - \rho_l g\nabla z\right]\right) - \rho_l q/V_{b,f} = 0. \tag{11}$$

It is worth noting that Eq. (11) is basically the same as Eq. (10) without the assumption of a constant fluid density. Although in pEDFM, the fracture cells are meshed in n-1 dimensions (where n is the number of dimensions of the reservoir system), the computation accounts for the fracture aperture and solves for the pressures in the centroids of these fracture cells. The use of non-neighboring connections facilitates the coupling between the matrix and fracture pressures and does not require applying fracture pressures as boundary conditions, as in other FEM approaches (where the fracture pressures are available only at the nodes).

2.3. Mechanical deformation of a pore-filled rock

The governing equation for the deformation of a pore-filled rock is the linear momentum balance equation (sometimes referred to as the equations of equilibrium, or quasi-static Cauchy equations of motion). It is given as:

$$\nabla\cdot\sigma + b = 0, \tag{12}$$

where σ is the total (Cauchy) stress tensor and b is the body force that acts on the formation. Using the modifications to Terzaghi's (Terzaghi et al., 1996) simple effective stress, modified effective stress can be defined as (Biot, 1941):

$$\sigma' = \sigma + \alpha p I, \tag{13}$$

where I is an identity matrix and p is the pore pressure. It is important to note that tensile stresses and strains are assumed positive in this work (engineering convention). Hooke's law provides the constitutive relationship between stress and strain, as follows:

$$\sigma' = C : \epsilon, \tag{14}$$

where C is the fourth-order elastic stiffness tensor of the rock and *epsilon* is the second-order strain tensor. Substituting this into Eq. (12) yields the governing equation for the mechanical deformation of a pore-filled rock:

$$\nabla\cdot[C : \epsilon - \alpha p I] + b = 0. \tag{15}$$

3. Discretization

This section discusses how to discretize and solve the governing equations for coupled flow and deformation in naturally fractured reservoirs. The flow in the matrix and fractures are solved using pEDFM, while the mechanical deformation and hydraulic fracture propagation are solved using XFEM.

3.1. Discretization of the flow equation in the matrix

To solve the governing equation for fluid flow in the matrix, we discretize the partial differential Eq. (6) in time and space. We use the backward Euler (implicit) scheme for temporal discretization and the finite volume method (FVM) for spatial discretization. The discretization of Eq. (6) in time yields:

$$\rho_l^{n+1}\left[\phi_m c_l + \frac{(\alpha-\phi_m)}{K_s} + \frac{\alpha^2}{K_{dr}}\right]^{n+1}\left(\frac{p_m^{n+1}-p_m^n}{\Delta t}\right) + \rho_l^{n+1}\frac{\alpha}{K_{dr}}\left(\frac{\sigma_v^{n+1}-\sigma_v^n}{\Delta t}\right) - \nabla\cdot\left(\rho_l\frac{k_m}{\mu}\left[\nabla p_m - \rho_l g\nabla z\right]\right)^{n+1} - \left(\rho_l q/V_b\right)^{n+1} = R_m^{n+1}. \tag{16}$$

The subscripts n+1 and n in this equation refer to the current and previous time steps, respectively. Note that the zero on the right-hand side of Equation [6] has been replaced by the residual of the matrix flow equation (R_m) because the temporal discretization introduces truncation errors.

Next, we discretize Eq. (16) in space using FVM with two-point flux approximation (TPFA). This involves integrating the equation over a control volume that has a bulk volume, V_b. Lie (2019) presented an elegant implementation of the FVM using discrete divergence (div) and discrete gradient (grad) operators. Eq. (16) can be discretized spatially using these discrete operators to obtain:

$$V_b\rho_l^{n+1}\left[\phi_m c_l+\frac{(\alpha-\phi_m)}{K_s}+\frac{\alpha^2}{K_{dr}}\right]^{n+1}\left(\frac{p_m^{n+1}-p_m^n}{\Delta t}\right)+V_b\rho_l^{n+1}\frac{\alpha}{K_{dr}}\left(\frac{\sigma_v^{n+1}-\sigma_v^n}{\Delta t}\right)-div\left(\frac{\rho_l}{\mu}\left[T_{i,k}^{-1}+T_{k,i}^{-1}\right]^{-1}\left[grad\left(p_m\right)-\rho_l\, g\, grad\left(z\right)\right]\right)^{n+1}-\left(\rho_l q\right)^{n+1}=R_m^{n+1}, \tag{17}$$

where the div and grad operators are implemented in Lie (2019) as functions that multiply a sparse matrix (that is either a discrete divergence or a discrete gradient matrix) with a vector, such as p or z in this equation. The face transmissibility, $T_{i,k}$ is given as:

$$T_{i,k}=A_{i,k}K_i\frac{\vec{c_{i,k}}\cdot\vec{n_{i,k}}}{\left|\vec{c_{i,k}}\right|^2}, \tag{18}$$

where $\vec{n_{i,k}}$ represents the unit normal vector from the centroid of a cell, i to the interface between cells i and k, and $\vec{c_{i,k}}$ is the vector from the cell centroid to the face centroid. $T_{i,k}$ is the half-transmissibility, which represents the contribution of a cell to a face transmissibility. It is so-called because it entails the contribution of the two cells on the sides of each face of a cell in the simulation domain.

3.2. Fracture modeling using the pEDFM

Like EDFM, the projection-based EDFM simulates fractures as (n-1)-dimensional cells. The matrix is typically discretized independently of the fractures, using structured n-dimensional cells. This independence in the meshing of the matrix and fractures results in the embedment of the fracture cells in the matrix cells. Both pEDFM and EDFM account for the exchange of fluids between the matrix and fractures using the concept of non-neighboring connections and transmissibilities. In standard reservoir simulation, the concept of non-neighboring connections is used when a cell needs to exchange fluids with another cell that is not its topological neighbor. It involves the addition of a non-neighboring mass rate, q_{nnc} to the discretized governing matrix flow equation (17) as follows:

$$V_b\rho_l^{n+1}\left[\phi_m c_l+\frac{(\alpha-\phi_m)}{K_s}+\frac{\alpha^2}{K_{dr}}\right]^{n+1}\left(\frac{p_m^{n+1}-p_m^n}{\Delta t}\right)+V_b\rho_l^{n+1}\frac{\alpha}{K_{dr}}\left(\frac{\sigma_v^{n+1}-\sigma_v^n}{\Delta t}\right)-div\left(\frac{\rho_l}{\mu}\left[T_{i,k}^{-1}+T_{k,i}^{-1}\right]^{-1}\left[grad\left(p_m\right)-\rho_l g\, grad\left(z\right)\right]\right)^{n+1}-\left(\rho_l q\right)^{n+1}+\left(q^{nnc}\right)^{n+1}=R_m^{n+1}, \tag{19}$$

where q^{nnc} is the mass rate of the fluid that is exchanged across the NNC (in units of mass per time). The mass rate is given as:

$$q^{nnc}=\sum_{j=1}^{N_{nnc}}A_j^{nnc}\frac{k_j^{nnc}}{\mu}\rho\left[\frac{(p-\rho g z)-(p-\rho g z)_j^{nnc}}{d_j^{nnc}}\right]. \tag{20}$$

Here, subscript j refers to the index of the current non-neighboring connection and ranges from one to the total number of NNCs (N_{nnc}). The two quantities in the numerator of the last term are the flow potentials of the current cell and that of its non-neighboring cell. We represent the permeability, area, and distance of the NNCs by k^{nnc}, A^{nnc}, and d^{nnc}, respectively. The transmissibility of an NNC can be estimated as:

$$T^{nnc}=\frac{k^{nnc}A^{nnc}}{d^{nnc}}, \tag{21}$$

where the expressions for k^{nnc}, A^{nnc}, and d^{nnc} are unique to each type of NNC. In EDFM, we can have up to four different transmissibilities. These include the standard transmissibility between pairs of neighboring matrix cells, the standard transmissibility between pairs of neighboring fracture cells that are part of the same fracture plane, the non-neighboring transmissibility between a matrix cell and an embedded fracture cell, and the non-neighboring transmissibility between two fracture cells that are part of two different fracture planes. We refer the reader to Moinfar et al. (2013) for more details on each of these EDFM NNCs. Here, we only provide the equations needed to obtain the non-neighboring transmissibilities. The standard transmissibilities are computed as part of the flux term (the div() term) in Eq. (19), while the non-neighboring transmissibilities are computed as follows:

1. ***Matrix-Fracture Connectivity:***
   The expressions for k^{nnc}, A^{nnc}, and d^{nnc} for this connectivity are given as:

   $$A^{nnc}=2A_f, \tag{22}$$

   $$k^{nnc}=\frac{k_m k_f}{k_m+k_f}, \tag{23}$$

   $$d^{nnc}=\frac{\int_v x_n dv}{V}, \tag{24}$$

   where, k_m is the matrix permeability, k_f is the fracture permeability, and A_f is the fracture area. The symbols x_n, dv, and v represent the normal distance of the element from the fracture, the volume element, and cell volume, respectively. The k^{nnc}, A^{nnc}, and d^{nnc} values computed from these equations are then used to compute the corresponding non-neighboring transmissibility using Eq. (21).
2. ***Intersecting Fracture Connectivity:***
   The non-neighboring transmissibility for this connectivity is given as:

   $$T^{nnc}=\frac{T_1T_2}{T_1+T_2}, \tag{25}$$

   where, T_1 and T_2 are the half transmissibilities of the two intersecting fractures:

   $$T_1=\frac{k_{f1}\omega_1 L_{int}}{d_{f1}}, \tag{26}$$

   $$T_2=\frac{k_{f2}\omega_{f2}L_{int}}{d_{f2}}. \tag{27}$$

   In these two equations, L_{int} represents the length of the line formed when two fracture cells intersect in a matrix cell, while ω_f and k_f are the fracture aperture and permeability, respectively. The symbols d_{f1} and d_{f2} represent the distances from the centroids of fracture cells 1 and 2 to the intersection line.

The projection-based embedded discrete fracture model can model fractures with low conductivities by including an NNC between a fracture and one of its two neighboring matrix cells in each direction. The determination of the matrix cell to be selected out of a pair of cells (in each direction) requires an algorithm. Jiang and Younis (2017) presented this algorithm for 2D systems, while Olorode et al. (2020) presented an algorithm for 3D systems. The matrix cells selected using this algorithm are referred to as the "projection cells", while the matrix cells that host the fracture cells are referred to as the "host cells". The projection-based EDFM adds two more NNCs to the EDFM connectivities. These are:

1. ***Projection Matrix/Fracture Transmissibility:***
The projection matrix/fracture (pM-F) transmissibility is the non-neighboring transmissibility between a projection matrix cell and a fracture cell. Ţene et al. (2017) gives the expression for this transmissibility as:

$$T^{nnc}_{pM-F} = \frac{A_{if\perp\vec{x}} k^{nnc}_{pM-F}}{d^{nnc}_{pM-F}}, \tag{28}$$

where,

$$k^{nnc}_{pM-F} = \frac{k_{pM} k_f}{k_{pM} + k_f}. \tag{29}$$

In this equation, $A_{if\perp\vec{x}}$ is the area of the fracture projections along the spatial directions. The symbol $\vec{x}$ represents the spatial coordinates (X and Y in 2D or X, Y, and Z in 3D), and d^{nnc}_{pM-F} is the distance between the centroid of the fracture and that of the projection cell.

2. ***Projection Matrix/Matrix Transmissibility:***
The projection matrix/matrix (pM-M) transmissibility is the transmissibility between a host matrix cell and its corresponding projection matrix cells. It is given as:

$$T^{nnc}_{pM-M} = k\frac{A_{ii} - A_{if\perp x}}{\Delta\vec{x}_e}, \tag{30}$$

where $\Delta\vec{x}_e$ refers to the grid block sizes in each spatial direction.

3.3. Discretization of the flow equation in the fracture

The fracture flow equation (11) is discretized in time and space using the backward Euler and finite volume methods to obtain:

$$\left(c_l\rho_l\phi_f\right)^{n+1}\frac{p_f^{n+1}-p_f^n}{\Delta t} - \nabla\cdot\left(\rho_l\frac{k_f}{\mu}\left[\nabla p_f - \rho_l g\nabla z\right]\right)^{n+1} - \left(\rho_l\, q/V_b\right)_f^{n+1} - \left(q^{nnc}\right)_f^{n+1} = R_f^{n+1}. \tag{31}$$

Integrating over the fracture bulk volume ($V_{b,f}$) and using the discrete div and $grad$ operators for the flux term (as in Section 3.1), we obtain:

$$\left(V_{b,f}c_l\rho_l\phi_f\right)^{n+1}\frac{p_f^{n+1,j}-p_f^n}{\Delta t} - div\left(\frac{\rho_l}{\mu}\left[T^{-1}_{i,k}+T^{-1}_{k,i}\right]^{-1}\left[grad\left(p_f\right)-\rho_l\, g\, grad\left(z\right)\right]\right)_f^{n+1,j} - \left(\rho_l\, q\right)_f^{n+1,j} - \left(q^{nnc}\right)_f^{n+1,j} = R_f^{n+1,j}. \tag{32}$$

Here, the bulk volume of each fracture cell is calculated as the product of the reservoir thickness, fracture length at the current time step, and fracture aperture at the current time step. The length and aperture of each fracture cell at the current time step are computed from the coupled solution of the flow and mechanical deformation problems, which are discussed in the next section.

3.4. Discretization of the linear momentum balance equation with XFEM

The governing equation for the conservation of linear momentum balance (12) can be expressed in the weak form by multiplying Eq. (12) by a test function $v(x,t)$, and integrating over a volume, Ω, to obtain:

$$\int_\Omega v\left(x,t\right)\left(\nabla\cdot\sigma + b\right)d\Omega = 0. \tag{33}$$

The Appendix presents the XFEM procedure to discretize this equation, as in Khoei (2014). The matrix form of the discretized equation is given as:

$$\begin{bmatrix} K_{uu} & K_{ua} \\ K_{au} & K_{aa} \end{bmatrix}\begin{Bmatrix} U \\ A \end{Bmatrix} = \begin{Bmatrix} F_u \\ F_a \end{Bmatrix}, \tag{34}$$

where each term in this equation is obtained from Eqs. (A.17)–(A.22) in Appendix.

4. A fixed-stress splitting algorithm to couple pEDFM and XFEM

A closer look at the n+1 and n subscripts in Eq. (19) indicates that this equation is written in the fully coupled form because the displacement and pressure are required at the current time step, n+1. The solution of the fully coupled form of the equation typically involves the use of a Newton–Raphson iterative scheme, which involves another loop within the time-stepping loop. As mentioned in the introduction, this work uses fixed-stress splitting, which is an unconditionally stable and convergent iterative coupling scheme. Like in the Newton–Raphson scheme, the fixed-stress splitting approach involves another loop within the time-stepping loop. However, in this inner loop, we fix the derivative of the mean volumetric stress with respect to time while solving the matrix flow equation for pressure (Kim, 2010). The fixed-stress approach allows us to keep the derivative of volumetric stress constant, as follows:

$$\frac{\partial\sigma_v}{\partial t} = \frac{\sigma_v^{n+1,j-1}-\sigma_v^n}{\Delta t}, \tag{35}$$

where j and j-1 are the current and previous indices of the inner loop for the fixed-stress splitting approach. Substituting Eq. (35) into Eq. (19) yields:

$$V_b\rho_l^{n+1,j}\left[\phi_m c_l + \frac{(\alpha-\phi_m)}{K_s} + \frac{\alpha^2}{K_{dr}}\right]^{n+1,j}\left(\frac{p^{n+1,j}-p^n}{\Delta t}\right) + V_b\rho_l^{n+1,j}\frac{\alpha}{K_{dr}}\left(\frac{\sigma_v^{n+1,j-1}-\sigma_v^n}{\Delta t}\right) - div\left(\frac{\rho_l}{\mu}\left[T^{-1}_{i,k}+T^{-1}_{k,i}\right]^{-1}\left[grad\,(p)-\rho_l\, g\, grad\,(z)\right]\right)^{n+1,j} - \rho_l^{n+1,j}q + (q^{nnc})^{n+1,j} = R_m^{n+1,j}. \tag{36}$$

From linear poroelasticity (in engineering convention, where tensile stresses and strains are positive):

$$\sigma_v + \alpha p = K_{dr}\epsilon_v. \tag{37}$$

In discretized form:

$$\sigma_v^{n+1,j-1} + \alpha p^{n+1,j-1} = K_{dr}\epsilon_v^{n+1,j-1}, \tag{38}$$

$$\sigma_v^n + \alpha p^n = K_{dr}\epsilon_v^n. \tag{39}$$

Therefore, Eq. (36) can be written as:

$$V_b\rho_l^{n+1,j}\left[\phi_m c_l + \frac{(\alpha-\phi_m)}{K_s} + \frac{\alpha^2}{K_{dr}}\right]^{n+1,j}\left(\frac{p^{n+1,j}-p^n}{\Delta t}\right) + V_b\rho_l^{n+1,j}\frac{\alpha}{K_{dr}}\left(\frac{K_{dr}\epsilon_v^{n+1,j-1} - \alpha p^{n+1,j-1} - K_{dr}\epsilon_v^n + \alpha p^n}{\Delta t}\right) - div\left(\frac{\rho_l}{\mu}\left[T^{-1}_{i,k}+T^{-1}_{k,i}\right]^{-1}\left[grad\,(p)-\rho_l g grad\,(z)\right]\right)^{n+1,j} - \rho_l^{n+1,j}q + (q^{nnc})^{n+1,j} = R_m^{n+1,j}. \tag{40}$$

Considering that volumetric strain is the sum of the diagonal entries in the strain tensor, it is given as:

$$\epsilon_v = \left[\epsilon_x\ \epsilon_y\ \epsilon_{xy}\right]\ [1\ 1\ 0]^T. \tag{41}$$

Defining vector m as $[1\ 1\ 0]^T$, the volumetric strain can be written in terms of Eq. (A.8) as:

$$\epsilon_v = (B^T m)^T U, \tag{42}$$

where $B = \left[B^{std}(x) \quad B^{enr}(x)\right]$ in Eq. (A.8). Substituting Eqs. (41) and (42) into Eq. (40) yields:

$$\begin{aligned} V_b\rho_l^{n+1,j}\left[\phi_m c_l + \frac{(\alpha-\phi_m)}{K_s}\right]^{n+1,j} p^{n+1,j} + V_b\rho_l^{n+1,j}\left[\frac{\alpha^2}{K_{dr}}\right]^{n+1,j} p^{n+1,j} \\ -V_b\rho_l^{n}\left[\phi_m c_l + \frac{(\alpha-\phi_m)}{K_s}\right]^{n} p^{n} \\ +V_b\rho_l^{n+1,j-1}\alpha(B^T m)^T\, u^{n+1,j-1} - V_b\rho_l^{n}\alpha\,(B^T m)^T u^{n} \\ -V_b\rho_l^{n+1,j-1}\left[\frac{\alpha^2}{K_{dr}}\right]^{n+1,j-1} p^{n+1,j-1} \\ -\Delta t\, div\left(\frac{\rho_l}{\mu}\left[T_{i,k}^{-1}+T_{k,i}^{-1}\right]^{-1}\left[grad\,(p) - \rho_l g\, grad\,(z)\right]\right)^{n+1,j} \\ -\left(\rho_l q\right)_m^{n+1,j}\,\Delta t + (q^{nnc})^{n+1,j}\,\Delta t = R_m^{n+1,j}. \end{aligned} \tag{43}$$

The discretized fracture flow Eq. (32) is implicitly a function of the matrix displacement because the fracture bulk volume is the product of the thickness, aperture, and length of each fracture cell at the current time step $(n+1)$ and current non-linear iteration, j. This aperture is obtained from the XFEM solution for the enriched displacements. In contrast, we obtain the length of the propagating fracture cell from the fracture propagation model presented in the next section. Considering the negligible volume of the fracture in comparison to the matrix, the change in the fracture volume is captured via its specification at the current time step and current non-linear iteration. It is written as:

$$\begin{aligned} V_{b,f}^{n+1,j} c_l \left(\rho_l\phi_f\right)^{n+1,j}\left(p_f^{n+1,j} - p_f^{n}\right) \\ -\Delta t\; div\left(\frac{\rho_l}{\mu}\left[T_{i,k}^{-1}+T_{k,i}^{-1}\right]^{-1}\left[grad\,(p_f) - \rho_l\, g\, grad\,(z)\right]\right)_f^{n+1,j} \\ -\left(\rho_l q\right)_f^{n+1,j} - (q^{nnc})_f^{n+1,j}\,\Delta t = R_f^{n+1,j}, \end{aligned} \tag{44}$$

We can define a pressure vector, p, which combines the matrix pressure p_m and fracture pressure p_f as follows:

$$p = \begin{Bmatrix} p_m \\ p_f \end{Bmatrix}. \tag{45}$$

Assuming that the fluid density in the matrix and fracture is constant, we can rewrite the combined discretized flow equations for the matrix and fracture in matrix form as:

$$\left(C_s + S - T\Delta t\right) p^{n+1,j} \approx C_s p^{n} + Q\left(u^{n+1,j-1} - u^{n}\right) + S p^{n+1,j-1} + f_l \Delta t, \tag{46}$$

where,

$$C_s = V_b\left(\phi_m c_l + \frac{\alpha-\phi_m}{K_s}\right)\ (for\ matrix), \tag{47}$$

$$C_s = V_b\phi_f c_l\ (for\ fracture),$$

$$S = V_b\left(\frac{\alpha^2}{K_{dr}}\right)\ (for\ matrix), \qquad S = 0\ (for\ fracture), \tag{48}$$

$$Q = \alpha(B^T m)^T\ (\text{for matrix}), \tag{49}$$

$$Tp = div\left(\frac{1}{\mu}\left[T_{i,k}^{-1}+T_{k,i}^{-1}\right]^{-1}\left[grad\,(p) - \rho_l\, g\, grad\,(z)\right]\right)^{n+1,j} \pm (q^{nnc})^{n+1,j}, \tag{50}$$

$$f_l = q. \tag{51}$$

Note that the displacements are solved at the nodes or vertices of the matrix cells (using XFEM), while the pressure solutions (from FVM) are obtained at the cell centroids. This explains why the Q term in Eq. (46) is based on the finite element method, whereas the other terms are based on the finite volume discretization of the flow equation. Additionally, the use of pm in Eq. (50) to account for the fact that we need to add the q^{nnc} term to the matrix flow equation but subtract it from the fracture flow equation. This ensures the conservation of mass as fluid is exchanged between the matrix and fracture. We can rewrite the matrix form of the discretized linear momentum balance Eq. (A.23) in a more compact form as:

$$Ku^{n+1,j} = b_m + Q^T p^{n+1,j-1}, \tag{52}$$

where the element stiffness matrix (K) is given as:

$$K = \begin{bmatrix} K_{uu} & K_{ua} \\ K_{au} & K_{aa} \end{bmatrix}, \tag{53}$$

the displacement vector containing both the standard and enriched displacements (u) is given as:

$$u = \begin{Bmatrix} U \\ A \end{Bmatrix}, \tag{54}$$

and the right-hand side is given as:

$$b_m = \begin{Bmatrix} F_u \\ F_a \end{Bmatrix}. \tag{55}$$

The two systems of equations to be solved sequentially in the fixed-stress splitting approach are Eqs. (46) and (52). Eq. (46) is first solved for $p^{n+1,j}$, after which this pressure solution is set to $p^{n+1,j-1}$, and used to find the displacement at the current time step (n+1) and current fixed-stress iteration j in Eq. (52). This displacement $u^{n+1,j}$ is then set to $u^{n+1,j-1}$ and used in the next calculation of pressure $p^{n+1,j}$ in Eq. (46). This fixed-stress loop is continued until we converge on a solution for pressure and displacement. The algorithm is summarized in the first six steps of the flow chart presented in Fig. 1.

4.1. Modeling of fracture propagation

As shown in Fig. 1, this work involves the modeling of fracture propagation using linear elastic fracture mechanics, where a fracture propagates if the stress intensity factor exceeds the critical stress intensity factor. I use the J-integral to compute the strain energy release rate (or work /energy per unit fracture surface area) of a material. For isotropic linear elastic materials, the J-integral can be directly related to the fracture toughness as (Rice, 1968):

$$J = \int_{\Gamma}\left(W\,dy - t\cdot\frac{\partial u}{\partial x}ds\right), \tag{56}$$

where $W(x,y)$ is the strain energy density, t is the surface traction vector, and u is the displacement vector. The J integral can be related to stress intensity factor as follows (for mode I plane strain model) (Rice, 1968) :

$$J_I = K_I\frac{2\left(1-\nu^2\right)}{E}. \tag{57}$$

For mode II, the J integral is given as (Yoda, 1980):

$$J_{II} = K_{II}\frac{2\left(1-\nu^2\right)}{E}. \tag{58}$$

Here, ν is the Poisson's ratio and E is the Young's modulus of the material. To determine the direction of fracture propagation, we calculate the propagation angle using the maximum circumferential stress criterion as follows (Khoei, 2014):

$$\theta_c = 2tan^{-1}\frac{1}{4}\left(\frac{K_I}{K_{II}} - sign\left(K_{II}\right)\sqrt{\left(\frac{K_I}{K_{II}}\right)^2 + 8}\right) \tag{59}$$

To find the propagation length we use the secant method as in Zeng et al. (2018). This is a two-step iterative procedure, which is used to calculate propagation length based on two prescribed initial guesses as follows:

$$\delta l = l_{02}^2 - \frac{f\left(l_{02}\right)\left(l_{02}-l_{01}\right)}{f\left(l_{02}\right) - f\left(l_{01}\right)}. \tag{60}$$

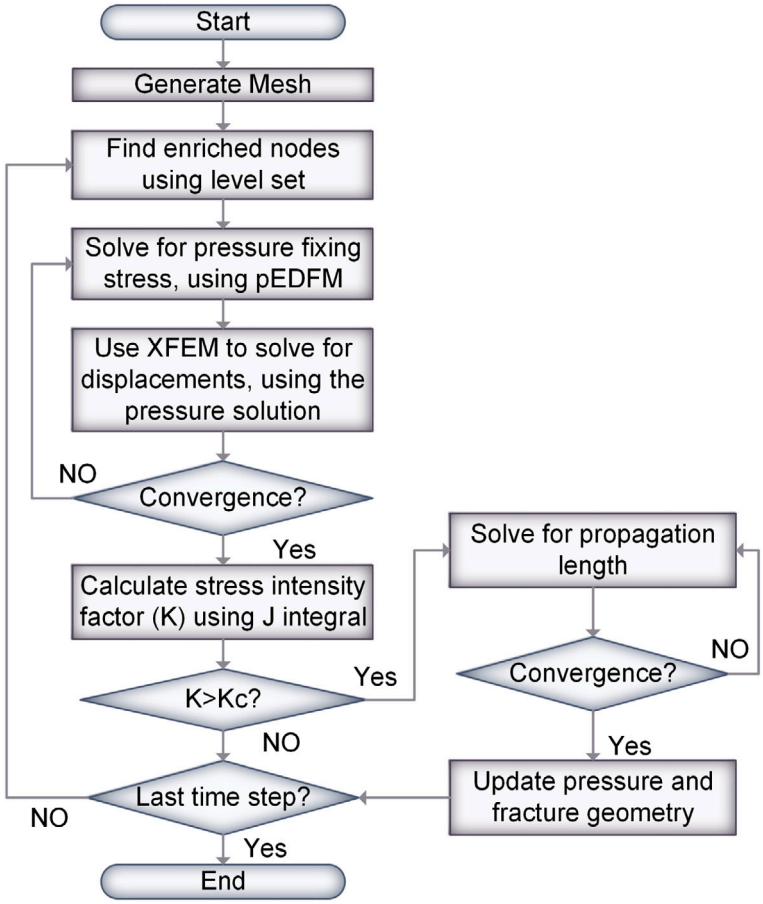

Fig. 1. Algorithm for coupled flow and geomechanics using the fixed-stress approach.

Here, δl is the propagation length and l_{01} and l_{02} are two initial guesses for propagation length. The stress intensity factor is calculated in this process as a function of the propagation length:

$$f(\delta l) = K_I - K_{Ic} = 0, \tag{61}$$

where K_I is the stress intensity factor calculated using the J integral as a function of propagation length, and K_{Ic} is the critical stress intensity factor, which is a material property. As indicated in Fig. 3, the solver for the fracture propagation iteratively evaluates the stress intensity factor as a function of the fracture propagation length until convergence is achieved.

This section focuses on the verification of our numerical simulation model by comparing the model results against published analytical solutions in the literature. To validate the coupled flow and deformation model, we present comparisons of our simulation results to the Terzaghi's one-dimensional (1D) consolidation problem (Terzaghi et al., 1996) and the two-dimensional (2D) Mandel problem (Mandel, 1953). We then present the simulation results from a simulation of fluid injection into a crack which is not allowed to propagate to evaluate the accuracy of the numerical model in predicting the opening of the crack. Next, we validate the modeling of crack opening by applying tensile forces on the boundary of a domain with an initial crack. Given the accurate match of all these cases against published analytical solutions, we proceed to model a case with a hydraulic fracture in the middle of two long sealing natural fractures to illustrate the importance of using pEDFM instead of EDFM in low-conductivity fractures. We conclude this paper with a model of a case with coupled flow, geomechanics, fracture propagation and opening, which is compared against published analytical solutions.

4.2. The Terzaghi problem

The iteratively coupled flow and deformation model developed is validated with the Terzaghi 1D consolidation problem. The physical model shown in Fig. 2(a) consists of a homogeneous porous formation that is subjected to a constant load, σ at the top. We only model half of the height of the domain because of symmetry, so we applied a no-flow boundary condition at the bottom and side of the sample while the top is fully drained. The displacements are fixed at the bottom and the roller boundary condition is applied on both vertical sides. Table 1 summarizes the model parameters used in the analytical and numerical simulation of the Terzaghi's problem. Fig. 2(b) shows that Our numerical simulation results match the analytical solution very closely. Each curve in this figure corresponds to the pressure profile at an instance in time. The results show that the pressure builds up instantaneously when the load is applied at time, t = 0, but as time evolves, the pressure dissipates due to the flow of fluid out of the top and bottom faces of the full domain with height, 2 h.

4.3. The Mandel problem

The Mandel problem involves modeling the non-monotonic pressure variation expected when a poroelastic material is subjected to a constant vertical load and allowed to drain on its lateral sides, as shown in Fig. 3. We simulate the top right quarter of the domain (due to symmetry) as shown in Fig. 3(b). The flow boundary conditions are such that the right side is drained with a constant pressure of zero whereas all other three sides are modeled as no-flow boundaries. The mechanical boundary conditions used in this quarter domain are shown in the Fig. 3(b). We modeled the top as a rigid motion boundary

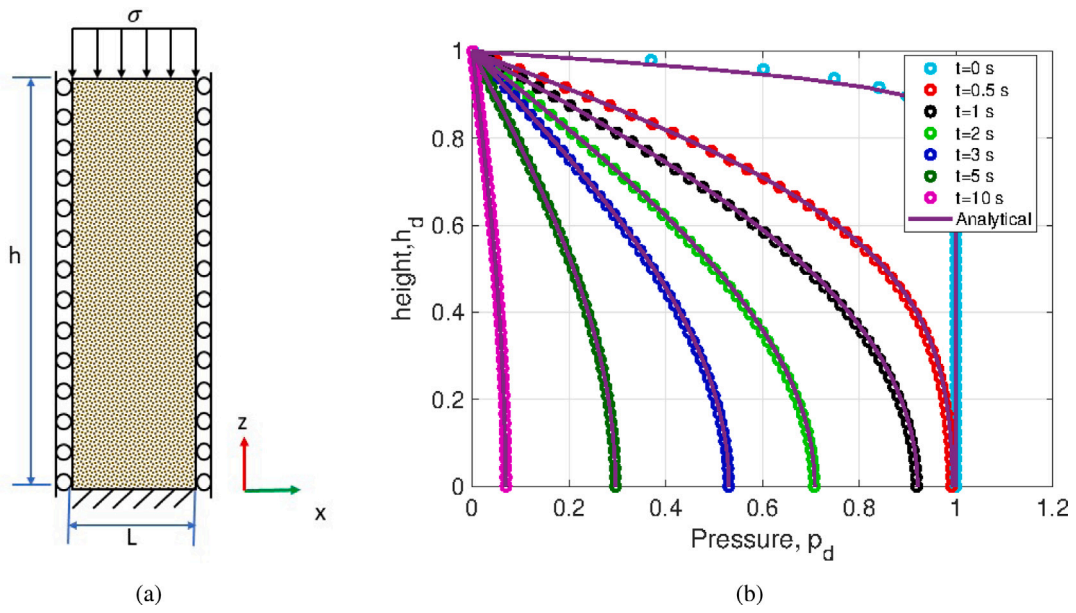

Fig. 2. Image shows the sketch of the description of the Terzaghi problem on the left and the comparison of pressure profile with the analytic solution on the right.

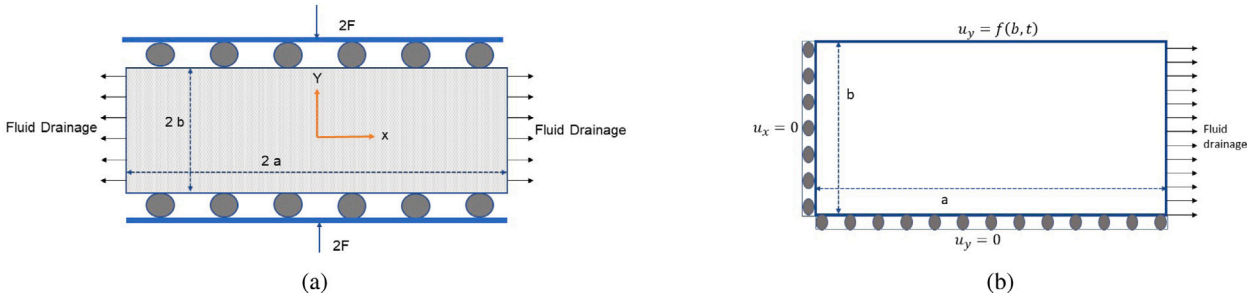

Fig. 3. Sketch of the description of the Mandel problem (Left). Sketch of simulation domain with boundary conditions (Right).

Table 1
Input parameters for the Terzaghi's problem.

Input data	Value	Unit
Number of grid	$1 \times 49 \times 1$	–
Physical domain dimensions	$1 \times 45 \times 1$	m
Porosity	0.25	–
Permeability	50×10^{-15}	m^2
Young's modulus	1×10^6	Pa
Poisson's ratio	0.2	–
Biot's coefficient	1	–
Overburden pressure	20×10^3	Pa
Fluid viscosity	1×10^{-3}	pa – s
Fluid compressibility	4×10^{-10}	1/Pa
Initial Pressure	1×10^7	Pa

Table 2
Input parameters for the Mandel problem.

Input data	Value	Unit
Number of grid	$50 \times 25 \times 1$	–
Physical domain dimensions	$10 \times 5 \times 1$	m
Porosity	0.2	–
Permeability	5×10^{-13}	m^2
Young's modulus	1×10^6	Pa
Poisson's ratio	0.2	–
Biot's coefficient	1	–
Overburden pressure	2.5×10^6	Pa

condition by computing the Y-component of displacement (uy) which maintains a deformation equal to the analytic deformation at the nodes on the top surface of the simulation domain, as in Chukwudozie (2016). The deformation of the sample should be confined to the plane strain conditions, so that no deformation is allowed in the direction normal to the plane shown in 3. Verruijt (2013) discusses the Mandel problem in more detail, and provides the analytical solution, which was first presented by Mandel (1953).

Table 2 summarizes all the model parameters used in the analytical and numerical simulation of the Mandel problem. Fig. 4 provides a comparison of our numerical simulation results to the analytical solution. It shows that our model can capture the Mandel–Cryer effect, where the pressure at the middle of the sample first rises before eventually declining to the zero-pore pressure value specified at the lateral boundaries, as in Fig. 4(a). This explains the observed non-monotonic pressure variation in both the analytical and numerical solutions.

4.4. Crack evolution due to injection

Having verified the ability of our coupled flow and geomechanics model to reproduce known analytical solutions, we proceed to validate its accuracy when strong discontinuities like fractures or faults are present in the domain. In this subsection, we simulate fluid injection into a fracture in the middle of the rectangular domain shown in Fig. 5. All four boundaries of the domain are modeled as a pin boundary condition (that is, all components of the displacement vector are set to zero). We summarize the model parameters used in Table 3. To

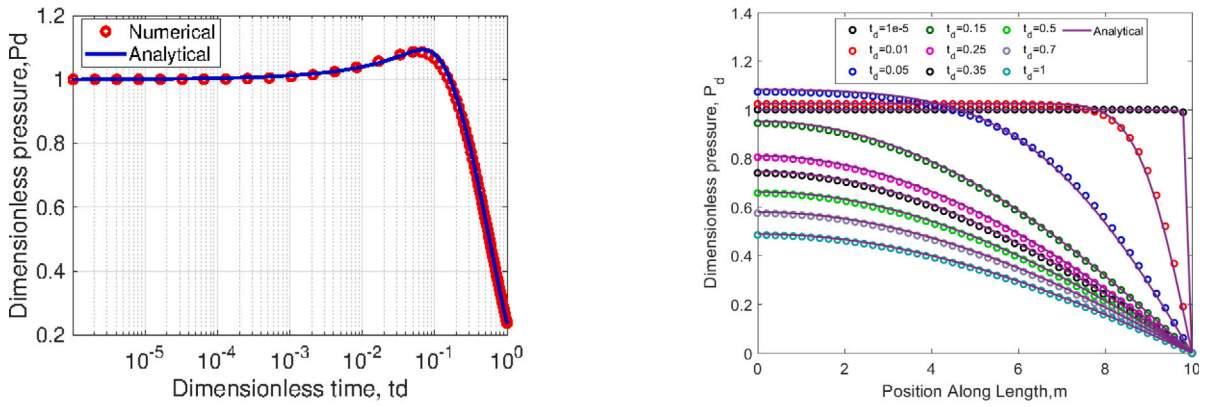

Fig. 4. Comparison of the pressure profile with Mandel's analytical solution at the middle of the full domain (Left), and along the length from the center of the full domain to the right boundary (Right).

Table 3
Input parameters for the crack evolution problem.

Input data	Value	Unit
Number of grid	$50 \times 50 \times 1$	–
Physical domain dimensions	$50 \times 50 \times 1$	m
Matrix porosity	0.2	–
Matrix permeability	9.87×10^{-20}	m^2
Young's modulus	20×10^9	Pa
Poisson's ratio	0.25	–
Biot's coefficient	1	–
Overburden pressure	2.5×10^6	Pa
Initial fracture length	3	m

Table 4
Input parameters for the simulation of a crack under tension.

Input data	Value	Unit
Number of grid	$50 \times 50 \times 1$	–
Physical domain dimensions	$5 \times 5 \times 1$	m
Young's modulus	20×10^9	Pa
Poisson's ratio	0.25	–
Biot's coefficient	1	–
Initial fracture length	1.1	m
Applied tension load	1×10^6	Pa

obtain the results in Fig. 5(b), We specify the injection volume by injecting at a fixed rate. The simulated pressure in the fracture cells are then averaged and plotted against the injection volume. Chukwudozie (2016) extended the analytical solution from Sneddon and Lowengrub (1969) to account for quasi-static crack evolution under an injected fluid volume with no fluid loss to the formation, as follows:

$$p = \frac{E' V_{inj}}{2\pi L_0^2} + \sigma_{min}. \tag{62}$$

Here, p is the injected fluid pressure, L_0 is initial fracture length, σ_{min} is the minimum in-situ stress, V_{inj} is the injected fluid volume, and $E\prime$ can be defined as:

$$E' = \frac{E}{1-\nu^2}, \tag{63}$$

where, E and ν are Young's modulus and Poisson's ratio of the material, respectively. Eq. (62) shows a linear relationship between the injection pressure and volume at constant fracture length. Here, we only model the opening of the crack (that is, increasing aperture) but do not allow the fracture to propagate (no increase in the fracture length). Fig. 5(b) shows the comparison of the fracture pressure obtained from the use of the cubic law and the porous media approach for modeling flow in fractures. It shows that the fracture pressure increases linearly in both cases as the injection volume increases. However, the porous media approach overestimates the pressure as it considers the fracture as a porous medium instead of a parallel plate. The increase of porosity value bring the numerical solution closer to the analytical pressure. However, it still fails to match even in 100% porosity value. Therefore we conclude, it is important to model open or unpropped fractures with the cubic law.

4.5. Center crack under uniform tension

In this subsection, we validate our extended finite element model by simulating the opening of a pre-existing crack by applying tensile stresses at the two opposite boundaries of the domain, as shown in Fig. 6(a). We validate our simulation results against the analytical solution presented by Janssen et al. (2006). This analytical solution relates the fracture opening to the applied tension as follows:

$$w_f = \frac{2T}{E}\sqrt{\left(\frac{L_0}{2}\right)^2 - x^2}. \tag{64}$$

Here, w_f is the fracture aperture at point x, while T is the tension applied on the top and bottom surfaces of the material. Table 4 summarizes the input parameters used while Fig. 6(b) compares our simulation results to the analytical solution. The plot shows that the simulation results (red circle) match the analytical solution (black line), which indicates the accuracy of our simulation model in estimating fracture opening under tensile stresses. The next subsection discusses the modeling of fracture opening because of fluid injection.

4.6. Verification of fracture propagation

The problem modeled in this section involves the injection of water into a pre-existing crack in the middle of a 2D domain shown in Fig. 7. Table 5 shows the parameters used in the numerical simulation and analytical models. The analytical solution for volume-driven fracture propagation from Sneddon and Lowengrub (1969) is given as:

$$\Delta l = \left(\frac{E' Q^2}{4\pi\, G_c}\right)^{1/3}. \tag{65}$$

Here, Q is the injection volume in m^3, G_c is the fracture toughness in Pa-m, and Δl is the fracture propagation length. The fracture pressure (p_f) can be calculated using the following equation:

$$p_f = \left(\frac{G_c E'}{\pi\, l_0^2}\right)^{1/2}, \tag{66}$$

where, l_0 is the initial fracture length. Fig. 8 shows the comparison of our numerical simulation results to this analytical solution. The plot

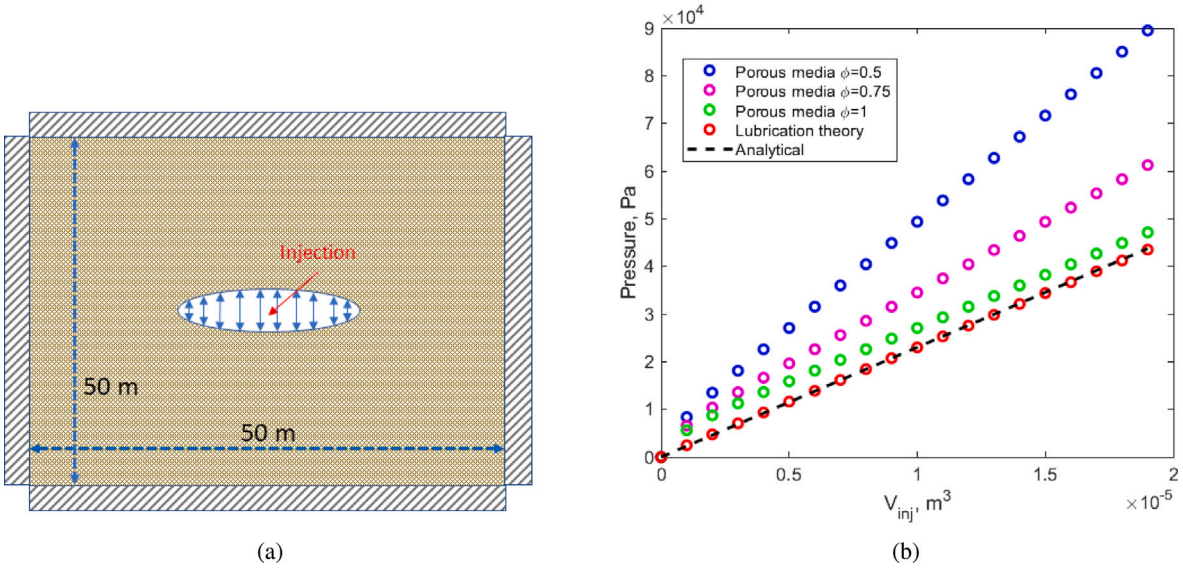

Fig. 5. This figure shows the simulation domain for the analysis of fracture opening due to injection (Left) and the comparison of pressure profile based on the cubic law and porous-medium formulation to the analytical solution (Right).

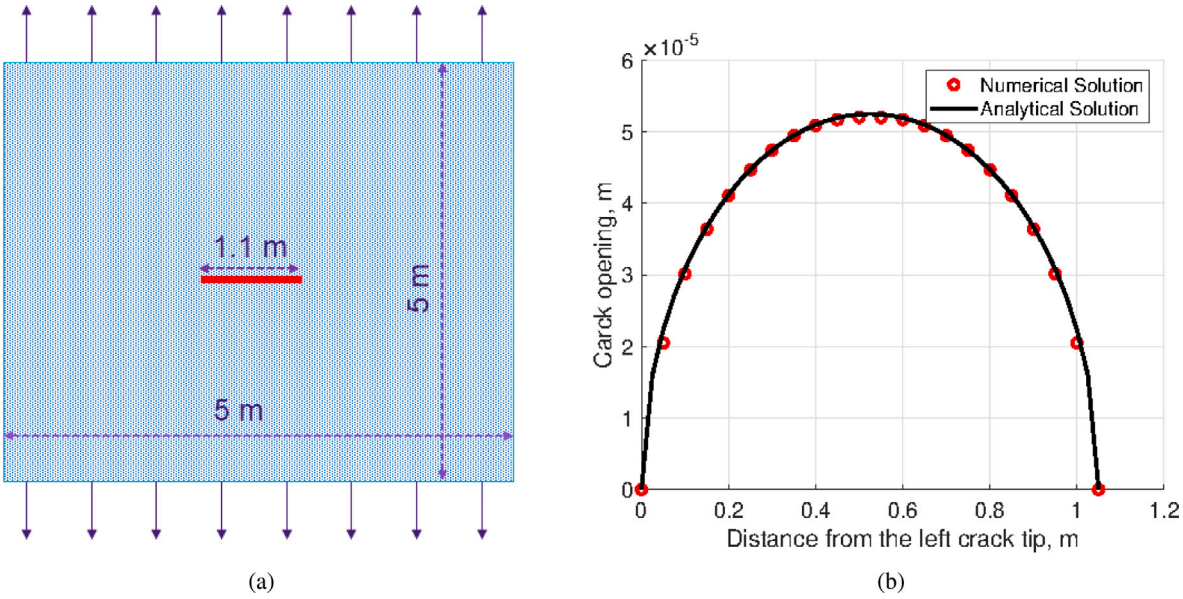

Fig. 6. A square plate with a pre-existing crack in the center (left). Crack opening comparison with analytical solution (Right).

of fracture pressure shows a linear increase with increasing injection volume until the volume reaches a critical value of $5 \times 10^{-5} m^3$. Beyond this volume, the fracture pressure drops as the fracture propagates, and its length increases as shown in Fig. 8(b). The plots of both fracture pressure and change in fracture length against injection volume shows a good match with the analytical solution.

5. Applications

5.1. Fracture opening at low fracture conductivity values

In this subsection, we focus on the application of our simulation model in reservoirs with low-conductivity fractures. This is important because EDFM is unable to model these kinds of fractures accurately, as discussed in the introduction. Additionally, the deposition of fine sands and cementing materials into fractures leads to the cementation of fractures and a subsequent reduction in fracture conductivity. This

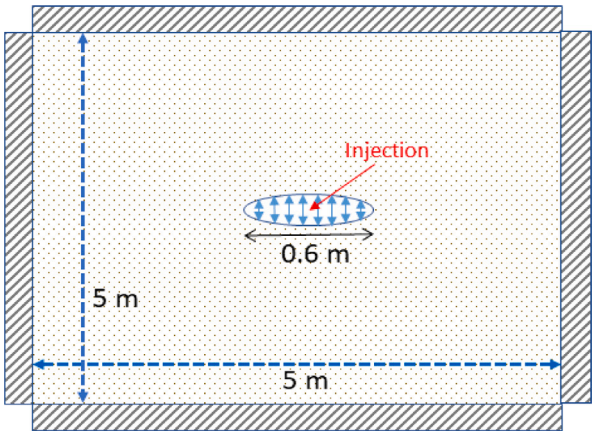

Fig. 7. Sketch of the simulation domain for fracture propagation.

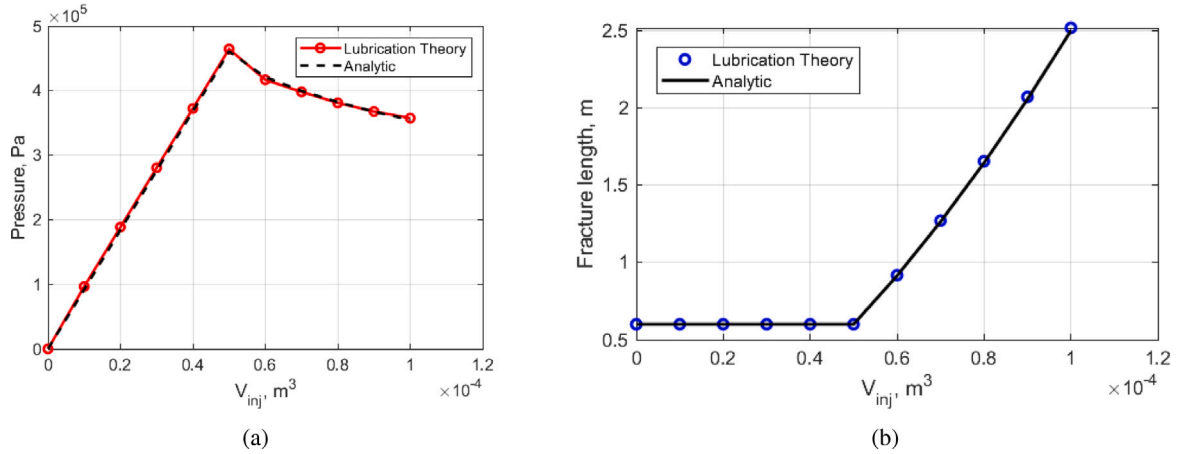

Fig. 8. Left plot shows the validation of the simulated fracture pressure against the analytical solution, whereas the right plot shows the validation of the simulated fracture length against the analytical solution.

Table 5
Input parameters for fracture propagation validation.

Input data	Value	Unit
Number of Grid	$50 \times 50 \times 1$	–
Physical domain dimensions	$5 \times 5 \times 1$	m
Young's modulus	20×10^9	Pa
Poisson's ratio	0.2	–
Biot's coefficient	1	–
Initial fracture length	0.6	m
Critical stress intensity factor	2039	$\text{Pa}\sqrt{\text{m}}$
Injection rate	1×10^{-5}	m^3/s
Fluid viscosity	1×10^{-3}	pa − s
Matrix permeability	9.8692×10^{-20}	m^2
Matrix porosity	0.2	–

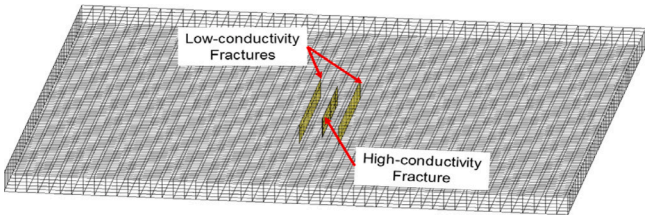

Fig. 9. This figure illustrates our simulation domain for the injection case. It shows a system with three fractures, where the conductive hydraulic fracture is in the middle of two sealing fractures.

(coupled with the orientation of fractures relative to that of the prevailing stress states) explains the common presence of low-conductivity fractures in unconventional reservoirs. To demonstrate that pEDFM is more appropriate than EDFM for modeling low-conductivity fractures, We simulate a reservoir with a high-conductivity fracture in the middle, and one low-conductivity fracture on each side of the middle fracture, as shown in Fig. 9. Table 6 shows the parameters used in this study. We inject fluid into the fracture in the center and calculate its change in fracture aperture with time. We compare our pEDFM-XFEM model results to those from an EDFM-XFEM model. The EDFM pressure profile on the left of Fig. 10 does not show the expected sealing effect of the two hydraulic fractures. Instead, its pressure front evolves through the domain with no restriction along its path. However, the pEDFM pressure profile on the right of the figure shows that the evolution of the pressure profile is curtailed by the sealing fractures on either side of the conductive fracture, as expected.

Figs. 11 and 12 show the corresponding difference in the X and Y components of the displacement vector for EDFM (left) and pEDFM (right). Both figures show that the extent of the deformation of the

Table 6
Input parameters for fracture opening at low-conductivity values.

Input data	Value	Unit
Number of Grid	$50 \times 50 \times 1$	–
Physical domain dimensions	$50 \times 50 \times 1$	m
Young's modulus	20×10^9	Pa
Poisson's ratio	0.2	–
Biot's coefficient	1	–
Conductive fracture length	10	m
Sealing fractures lengths	14	m
Injection rate	1×10^{-6}	m^3/s
Fluid viscosity	1×10^{-3}	pa − s
Matrix permeability	9.8692×10^{-14}	m^2
Matrix porosity	0.2	–
Sealing fracture permeability	9.8692×10^{-22}	m^2
Spacing between conductive and sealing fracture	1.75	m

material in the pEDFM model is smaller than in the EDFM model because of the sealing effect of the low-conductivity fractures. Fig. 13 compares the simulated fracture aperture from both models and indicates that the coupling of the EDFM and XFEM models underestimate fracture opening when compared with the pEDFM-XFEM modeling of the fractured well. The magnitude of this underestimation of fracture aperture is expected to increase as the fracture conductivity decreases and as the number of such sealing fractures (in the domain) increases. This will consequently lead to errors in the simulated production from such fractured reservoirs.

5.2. Fracture propagation in the presence of natural fractures

This subsection uses the coupled pEDFM-XFEM model to simulate the propagation of a hydraulic fracture in the presence of a pre-existing or natural fracture. Here, we placed a sub-vertical natural fracture in the vicinity of hydraulic fracture as shown in Fig. 14. The model parameters used in this analysis are outlined in Table 7. To evaluate the effect of the conductivity of the natural fracture on its interaction with the propagating fracture, we varied the natural fracture permeability from 10 nD to 100 mD.

To obtain the three simulation results shown in Figs. 15 and 16, the fracture permeabilities were set to 10 nD, 100 μD, and 100 mD for cases (a), (b), and (c), respectively. These figures show three distinct behaviors when the propagating fracture intersects the natural fracture. In Fig. 16(a) the hydraulic fracture propagates through the natural fracture without an observable change in the natural fracture pressure. This indicates that there is little or no leak-off of the injected fluid through this intersecting natural fracture. In contrast, Fig. 16(b) shows that the hydraulic fracture propagates through the natural fracture with

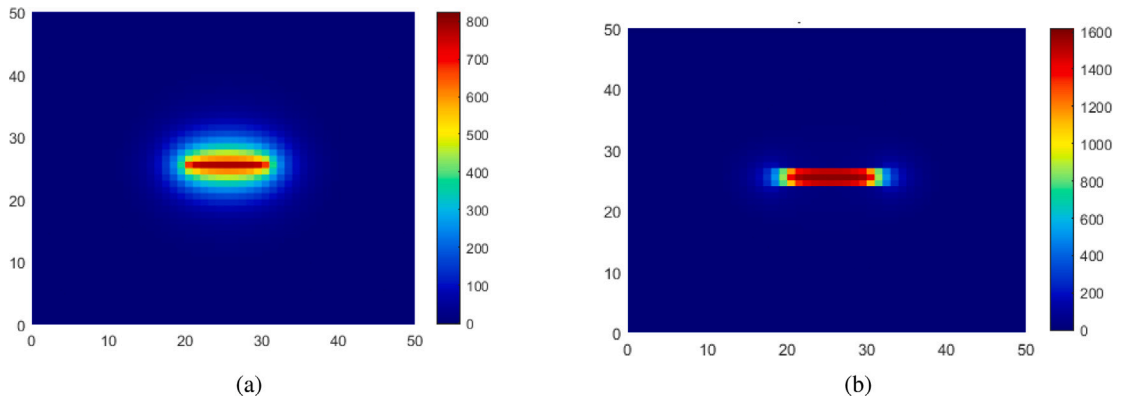

Fig. 10. Comparison of pressure (in *Psia*) profile for EDFM (left) and pEDFM (right).

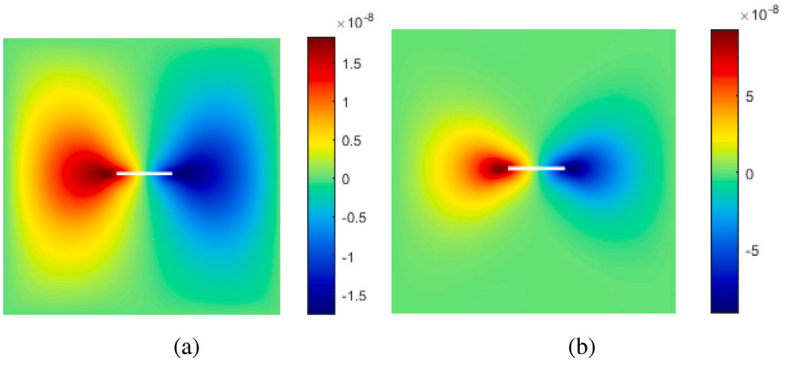

Fig. 11. Comparison between EDFM (left) and pEDFM (right) displacement profiles (in meters) in the x direction ($\mathbf{u}_x$).

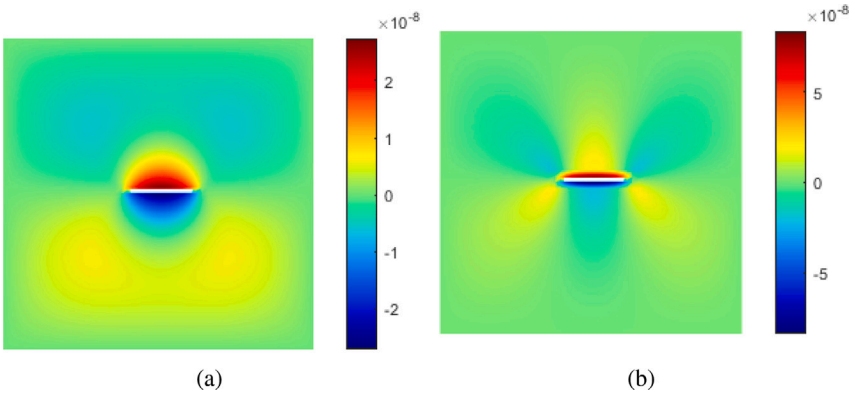

Fig. 12. Comparison between EDFM (left) and pEDFM (right) displacement profiles (in meters) in the Y direction ($\mathbf{u}_y$).

an observable increase in the natural fracture pressure. This pressure increase consequently indicates an observable fluid leak-off through the natural fracture. Finally, Fig. 16(c) indicates that the fluid leak-off is so high that the propagating hydraulic fracture gets "arrested", and is unable to propagate across the natural fracture. The flow of the injected fluid into the natural fracture disperses the pressure that was previously concentrated in the hydraulic fracture, resulting in a lower pressure, which is unable to sustain the propagation of the hydraulic fracture.

Fig. 17 shows the change of fracture pressure with time in the presence of a natural fracture with different conductivity values. The legend shows the different natural fracture permeability values, as well as a case in which the natural fracture is absent. The vertical magenta line indicates the time at which the propagating hydraulic fracture intersects the natural fracture. The results show that at a natural fracture permeability of less than 10μD, the hydraulic fracture propagates without observable fracture pressure changes. At natural fracture permeability values between 10μD and 1 mD, we observe two trends in the pressure profile after the hydraulic fracture intersects the natural fracture. The initial increase in pressure corresponds to the duration where the hydraulic fracture stops propagating, and pressure builds up in the natural fracture. In contrast, the subsequent decline in fracture pressure indicates that the fracture resumes its propagation. Finally, when the fracture permeability is above $\tilde{1}$00 mD, the increase in pressure observed indicates that the fracture stops propagating while the fracture pressure builds up. Fig. 18 illustrates the effect of the natural fracture conductivity on the aperture of the propagating hydraulic fracture. The point where these curves intersect the X-axis corresponds to the hydraulic fracture length. These results show that the hydraulic fracture aperture decreases as the natural fracture conductivity increases.

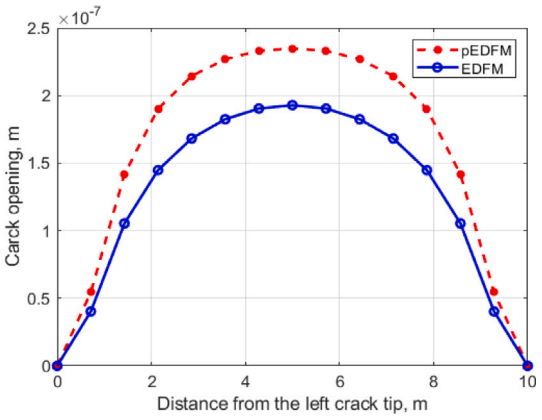

Fig. 13. Comparison of fracture opening. EDFM underestimates fracture opening in the presence of sealing fractures.

Table 7
Input parameters for hydraulic fracture propagation in the presence of a natural fracture case.

Input data	Value	Unit
Number of grids	$51 \times 51 \times 1$	–
Physical domain dimensions	$5.1 \times 5.1 \times 1$	m
Young's modulus	20×10^9	Pa
Poisson's ratio	0.2	–
Biot's coefficient	1	–
Initial hydraulic fracture length	0.75	m
Initial hydraulic fracture aperture	1×10^{-6}	m
Initial natural fracture length	2.75	m
Initial natural fracture aperture	1×10^{-6}	m
Injection rate	1×10^{-6}	m^3/s
Fluid viscosity	1×10^{-3}	$Pa - s$
Matrix permeability	9.8692×10^{-22}	m^2
Matrix porosity	0.2	–

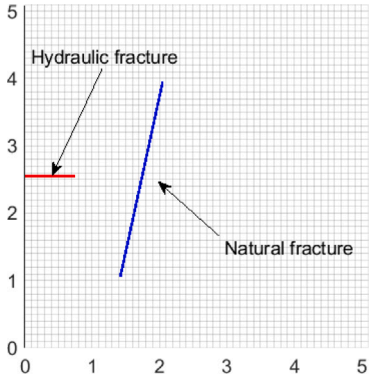

Fig. 14. Initial location of hydraulic and natural fractures before fluid injection.

5.3. Computational efficiency of the proposed numerical model

This subsection summarizes the computational performance of the proposed model on a 10-core Intel(R) Core (TM) i9-9820X CPU 3.31 GHz with 64 GB RAM. A total of 30 time steps were simulated in the fracture opening and propagation cases as shown in Fig. 19. The fracture propagation simulations ran for an average of 125 s, with 74% of the time spent in the propagation solver. The heights of the red, blue, purple, and green bars in Fig. 19 correspond to the number of nonlinear iterations taken before convergence in the cases presented in Figs. 5, 9, 8 and 14 respectively.

6. Conclusions

This work provides the first demonstration of the iterative coupling of pEDFM with XFEM to model hydraulic fracture propagation in naturally fractured reservoirs, such as unconventional oil and gas reservoirs. We used the fixed-stress splitting scheme to ensure the efficient and accurate modeling of the flow and mechanical deformation and fracture propagation in these fractured tight rocks. The use of pEDFM instead of EDFM allows modeling the interaction between hydraulic and natural fractures of any conductivity.

To demonstrate the accuracy of the proposed approach, we simulated several standard problems with known analytical solutions. We verified our coupling of flow and geomechanics by comparing our numerical simulation results to the analytical solutions of the Terzaghi and Mandel problems. We also simulated fracture opening and propagation and compared our model results to the published analytical solutions of Janssen et al. (2006) and Sneddon and Lowengrub (1969), respectively. All of these verification cases show an excellent match against published analytical solutions.

Using the proposed pEDFM-XFEM and an EDFM-XFEM model, we simulated a high-conductivity fractured well between two low-conductivity natural fractures to show the importance of modeling low-conductivity fractures accurately. The results show that EDFM-XFEM underestimates the fracture aperture and cannot model the displacement and pressure profiles accurately in reservoirs with low-conductivity fractures. Additionally, the comparison of the simulation results based on the cubic law, as well as that based on the common porous-medium assumption, to the analytical solutions from Sneddon and Lowengrub (1969) indicates that the common use of the latter could be inaccurate for flow in unpropped fractures. Finally, our simulation of the interaction between a propagating hydraulic fracture and a pre-existing natural fracture with different fracture permeability values indicates the role of the natural fracture conductivity in the interaction between both fractures.

CRediT authorship contribution statement

Harun Rashid: Methodology, Software, Validation, Visualization, Editing. **Olufemi Olorode:** Conceptualization, Review & editing, Supervision. **Chukwudi Chukwudozie:** Validation, Supervision.

Declaration of competing interest

The authors declare that they have no known competing financial interests or personal relationships that could have appeared to influence the work reported in this paper.

Acknowledgments

This work was facilitated by the use of the software packages available in the Craft and Hawkins Department of Petroleum Engineering at Louisiana State University (LSU) and the computational resources at the LSU Center for Computation and Technology (CCT).

Appendix. Discretization of the linear momentum balance equation with XFEM

To account for the presence of discontinuities in the domain, we use the following form of the divergence theorem, which accounts for these interior boundaries within the domain Khoei (2014):

$$\int_{\Omega} \nabla \cdot F \, d\Omega = \int_{\Gamma} F \cdot n_{\Gamma} d\Gamma - \int_{\Gamma_d} \left(F^{+} - F^{-}\right) \cdot n_{\Gamma_d} d\Gamma, \tag{A.1}$$

where F is any continuous function in the domain, whereas Γ and Γ_d represent the exterior and interior boundary surfaces of the domain, as

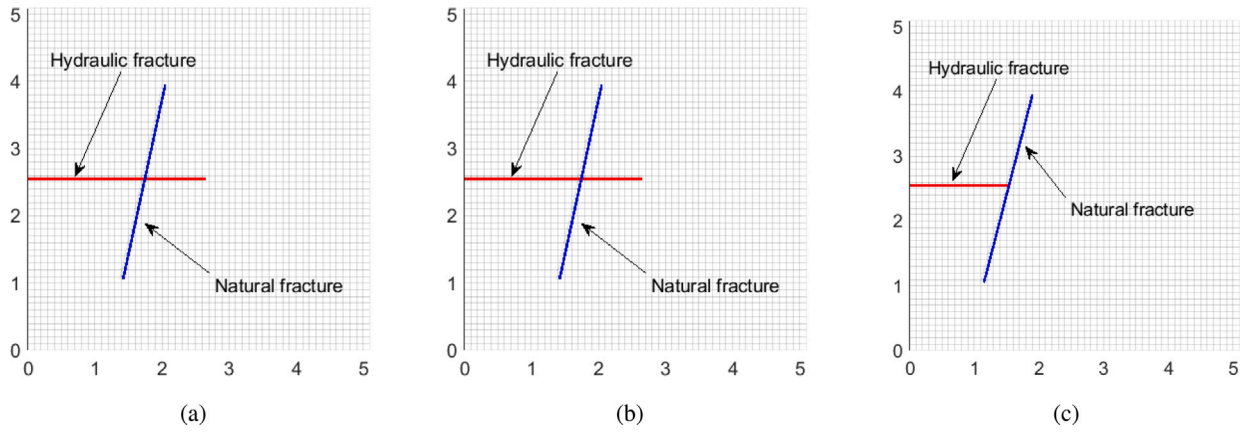

Fig. 15. Fracture location at the end of the simulation. In (a) and (b), the hydraulic fracture propagates through the natural fracture, whereas in (b) the propagating hydraulic fracture is "arrested" by the natural fracture.

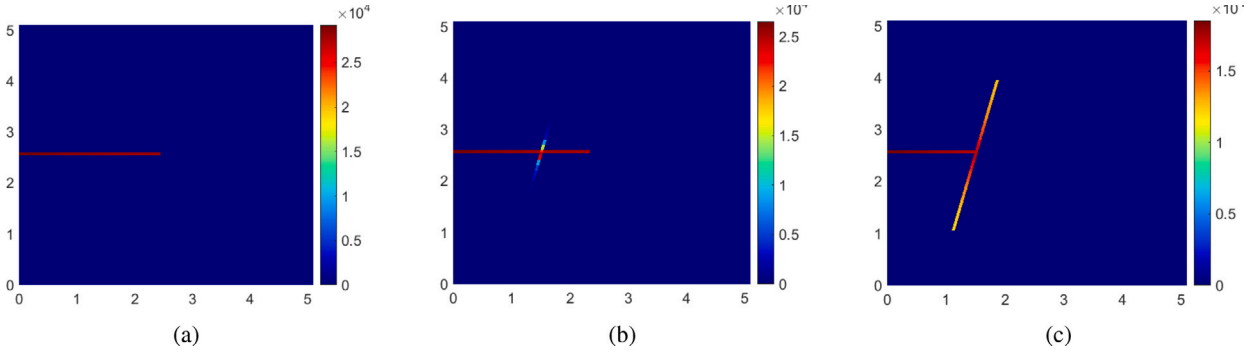

Fig. 16. The images show the pressure profile at the end of simulation. In (a), the hydraulic fracture propagates across the natural fracture without an observable change in the natural fracture pressure. In (b), the hydraulic fracture propagates through the natural fracture with an observable change in the natural fracture pressure. In (c), the propagating hydraulic fracture is "arrested" by the natural fracture.

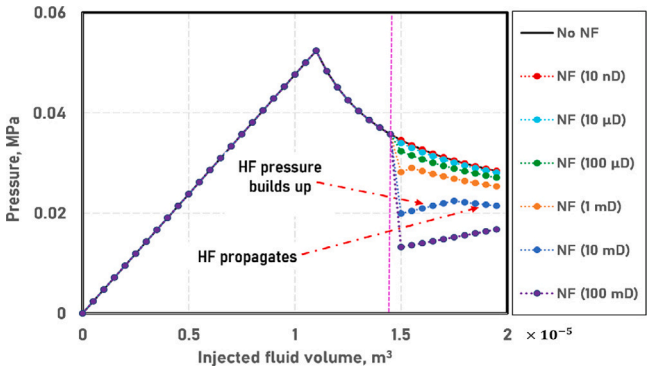

Fig. 17. Comparison of fracture pressures at different natural fracture conductivity values.

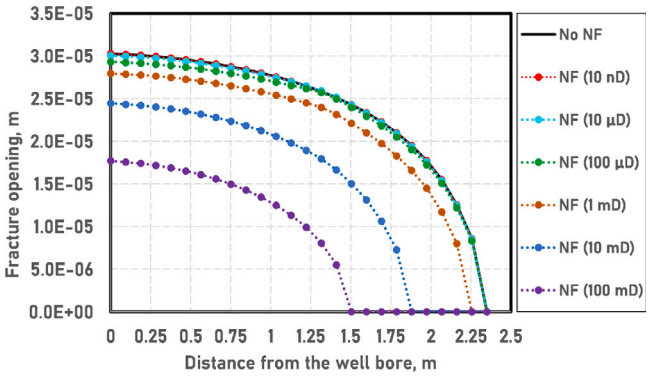

Fig. 18. Effect of natural fracture on fracture opening.

shown in Fig. A.1. Expanding Eq. (33) and applying this form of the divergence theorem yields:

$$\int_{\Omega} \nabla v : \sigma d\Omega + \int_{\Gamma_d} \left(v^{\pm} v^{-}\right) \cdot \sigma \cdot n_{\Gamma_d} d\Gamma - \int_{\Gamma} (v \cdot \sigma) \cdot n_{\Gamma} d\Gamma - \int_{\Omega} v \cdot b d\Omega = 0. \tag{A.2}$$

As in Khoei (2014), we impose the internal boundary condition on the discontinuity and substitute $\left(v^{\pm} v^{-}\right) = [[v]]$ to obtain:

$$\int_{\Omega} \nabla v : \sigma d\Omega + \int_{\Gamma_d} [[v \cdot \ \sigma]] \cdot \ n_{\Gamma_d} \, d\Gamma - \int_{\Gamma} v \cdot \bar{t} d\Gamma - \int_{\Omega} v \cdot b d\Omega = 0, \tag{A.3}$$

where the traction vector, $\bar{t}$ acts normal to the boundary (Γ). In the presence of fracture fluid, the second integral can be evaluated for strong discontinuities by imposing the internal boundary condition as follows:

$$\int_{\Gamma_d} [[v \cdot \ \sigma]] \cdot \ n_{\Gamma_d} \, d\Gamma = \int_{\Gamma_d} [[v \ ]] (\sigma \cdot n_{\Gamma_d}) \, d\Gamma = \int_{\Gamma_d} [[v \ ]] (-p \cdot n_{\Gamma_d}) d\Gamma, \tag{A.4}$$

where, p is the pressure inside the discontinuity. Substituting Eq. (A.4) into Eq. (A.3) yields:

$$\int_{\Omega} \nabla v : \sigma d\Omega - \int_{\Gamma_d} [[v \ ]] (p \cdot n_{\Gamma_d}) \, d\Gamma - \int_{\Gamma} v \cdot \bar{t} d\Gamma - \int_{\Omega} v \cdot b d\Omega = 0. \tag{A.5}$$

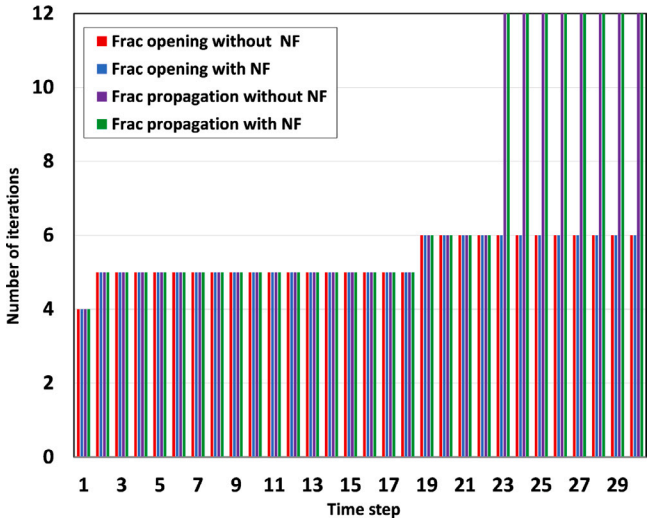

Fig. 19. Plot of the number of non-linear (fixed-stress) iteration against the time-step number indicates that the scheme converges after an average of 7.5 non-linear iterations.

To discretize this integral equation, we use XFEM, which enriches the standard finite element basis functions with Heaviside step functions (for crack surfaces) and asymptotic functions (for the crack tips). Considering the displacement field of an enriched element, u(x,t), the enriched approximation field can be expressed as:

$$u(x,t) = \sum_{i=1}^{n} N_i(x) U_i + \sum_{j=1}^{m} N_j(x) \left(\psi(x) - \psi\left(x_j\right)\right) A_j \equiv N^{std}(x) U + N^{enr}(x) A, \tag{A.6}$$

where, U_i represents the standard FEM displacement at the nodes, and A_j represents the corresponding displacement (or jump) which is calculated using the enriched functions. N_i and N_j are the standard and enriched shape functions, respectively, whereas ψ is the shifted enrichment function used in the enhanced approximation field. Similarly, the test function $v(x,t)$ can be defined in the same approximate space as the displacement field:

$$v(x,t) = \sum_{i=1}^{n} N_i(x) V_i + \sum_{j=1}^{m} N_j(x) \left(\psi(x) - \psi\left(x_j\right)\right) W_j \equiv N^{std}(x) V + N^{enr}(x) W, \tag{A.7}$$

where N^{std} is a vector with elements $N_i(x)$, and N^{enr} is a vector with elements $N_j(x)\left(\psi(x) - \psi\left(x_j\right)\right)$. In terms of the standard and enriched forms of the approximate displacement field, the strain vector is essentially the gradient of the standard and enriched displacement vector, and is given as:

$$\epsilon(x,t) = \sum_{i=1}^{n} \frac{\partial N_i}{\partial x} U_i + \sum_{j=1}^{m} \left[\frac{\partial N_j}{\partial x}\left(\psi(x) - \psi\left(x_j\right)\right)\right] A_j \equiv B^{std}(x) U + B^{enr}(x) A \equiv \begin{bmatrix} B^{std}(x) & B^{enr}(x) \end{bmatrix} \begin{Bmatrix} U \\ A \end{Bmatrix}. \tag{A.8}$$

Similarly, the variation of strain field is the gradient of the test function, (∇v), and is given as:

$$\nabla v(x,t) = \sum_{i=1}^{n} \frac{\partial N_i}{\partial x} V_i + \sum_{j=1}^{m} \left[\frac{\partial N_j}{\partial x}\left(\psi(x) - \psi\left(x_j\right)\right)\right] W_j \equiv B^{std}(x) V + B^{enr}(x) W = \begin{bmatrix} B^{std}(x) & B^{enr}(x) \end{bmatrix} \begin{Bmatrix} V \\ W \end{Bmatrix}. \tag{A.9}$$

Here, B_i^{std} and B_j^{enr} are the strain displacement matrices for the standard and enriched approximations, respectively. In 2D, they are defined as follows:

$$B_i^{std} = \begin{bmatrix} \partial N_i/\partial x & 0 \\ 0 & \partial N_i/\partial y \\ \partial N_i \partial y & \partial N_i \partial x \end{bmatrix} \tag{A.10}$$

$$B_j^{enr} = \begin{bmatrix} \partial N_j\left[\left(\psi \partial x - \psi\left(x_j\right)\right)\right]/\partial x & 0 \\ 0 & \partial N_j\left[\left(\psi \partial - \psi\left(x_j\right)\right)\right]/\partial y \\ \partial N_j\left[\left(\psi \partial x - \psi\left(x_j\right)\right)\right]/\partial y & \partial N_j\left[\left(\psi \partial x - \psi\left(x_j\right)\right)\right]/\partial x \end{bmatrix} \tag{A.11}$$

The discretized form of the extended finite element formulation can be obtained by substituting Eqs. (A.7) and (A.9) into Eq. (A.5) to obtain:

$$\int_{\Omega} \left(B^{std} V + B^{enr} W\right)^T \sigma d\Omega - \int_{\Gamma_t} [[\left(N^{std} V + N^{enr} W\right)^T]] p \cdot n_{\Gamma_d} d\Gamma - \int_{\Gamma_t} \left(N^{std} V + N^{enr} W\right)^T \vec{t} d\Gamma - \int_{\Omega} \left(N^{std} V + N^{enr} W\right)^T b \, d\Omega = 0 \tag{A.12}$$

Substituting the definition of strain in Eq. (A.8) into Hooke's law yields:

$$\sigma' = C\left[B^{std} U + B^{enr} A\right]. \tag{A.13}$$

Therefore, the total stress can be written as:

$$\sigma = C\left[B^{std} U + B^{enr} A\right] - \alpha p I. \tag{A.14}$$

Substituting this equation for total stress into Eq. (A.12) yields:

$$V^T \left[\int_{\Omega} \left(B^{std}\right)^T C B^{std} d\Omega\right] U + V^T \left[\int_{\Omega} \left(B^{std}\right)^T C B^{enr} d\Omega\right] A = V^T \left[\int_{\Omega} \left(B^{std}\right)^T \alpha p I \, d\Omega + \int_{\Gamma_t} [[\left(N^{std}\right)^T]] p \cdot n_{\Gamma_d} d\Gamma + \int_{\Gamma_t} \left(N^{std}\right)^T \vec{t} d\Gamma + \int_{\Omega} \left(N^{std}\right)^T b d\Omega\right], \tag{A.15}$$

and

$$W^T \left[\int_{\Omega} (B^{enr})^T C B^{std} d\Omega\right] U + W^T \left[\int_{\Omega} (B^{enr})^T C B^{enr} d\Omega\right] A = W^T \left[\int_{\Omega} (B^{enr})^T \alpha p I \, d\Omega + \int_{\Gamma_t} [[(N^{enr})^T]] p \cdot n_{\Gamma_d} d\Gamma + \int_{\Gamma_t} (N^{enr})^T \vec{t} d\Gamma + \int_{\Omega} (N^{enr})^T b d\Omega\right]. \tag{A.16}$$

This discrete system of equations can be written in the form, $KU - F = 0$ using the following definitions:

$$K_{uu} = \int_{\Omega} \left(B^{std}\right)^T C B^{std} d\Omega, \tag{A.17}$$

$$K_{ua} = \int_{\Omega} \left(B^{std}\right)^T C B^{enr} d\Omega, \tag{A.18}$$

$$F_u = \int_{\Omega} \left(B^{std}\right)^T \alpha p I \, d\Omega + \int_{\Gamma_t} [[\left(N^{std}\right)^T]] p \cdot n_{\Gamma_d} d\Gamma + \int_{\Gamma_t} \left(N^{std}\right)^T \vec{t} d\Gamma + \int_{\Omega} \left(N^{std}\right)^T b d\Omega, \tag{A.19}$$

$$K_{au} = \int_{\Omega} (B^{enr})^T C B^{std} d\Omega, \tag{A.20}$$

$$K_{aa} = \int_{\Omega} B^{enr^T} C B^{enr} d\Omega, \tag{A.21}$$

$$F_a = \int_{\Omega} (B^{enr})^T \alpha p I \, d\Omega + \int_{\Gamma_t} [[(N^{enr})^T]] p \cdot n_{\Gamma_d} d\Gamma + \int_{\Gamma_t} (N^{enr})^T \vec{t} d\Gamma + \int_{\Omega} (N^{enr})^T b d\Omega. \tag{A.22}$$

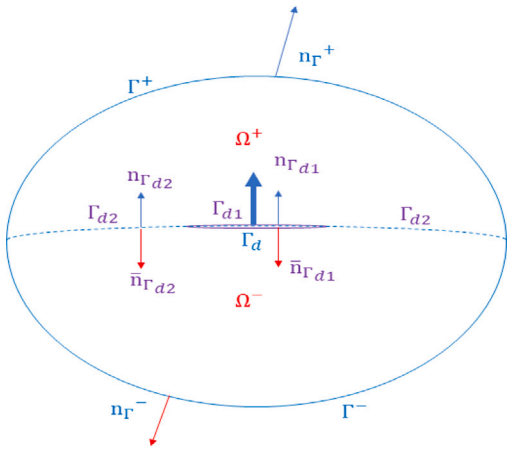

Fig. A.1. A two-dimensional domain Ω with an open discontinuity interface Γ_d. *Source:* Modified from Khoei (2014).

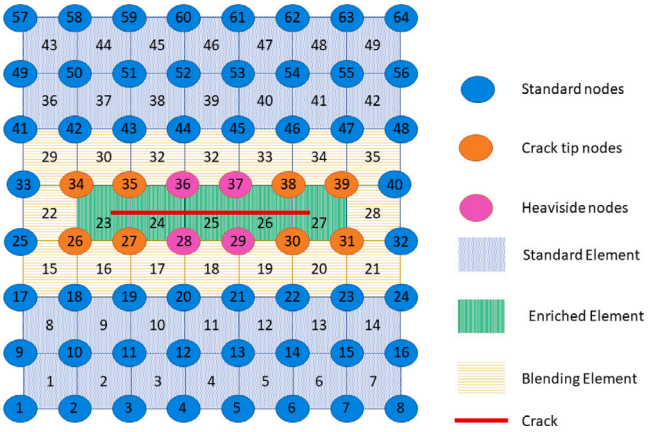

Fig. A.2. This sketch illustrates the classification of elements (and nodes) based on whether they are partially or completely cut through by a crack surface.

With $\vec{U}$ as the displacement vector $\vec{U} = [U\ A]^T$, the discrete system of Eqs. (A.15) and (A.16) can be written in matrix form as follows:

$$\begin{bmatrix} K_{uu} & K_{ua} \\ K_{au} & K_{aa} \end{bmatrix} \begin{Bmatrix} U \\ A \end{Bmatrix} = \begin{Bmatrix} F_u \\ F_a \end{Bmatrix} \tag{A.23}$$

For finite elements that are fully cut by a crack surface, we enrich the standard FEM approximation by adding Heaviside step functions of the form:

$$H(x) = \begin{pmatrix} +1 & if, x > 0 \\ -1 & if, x < 0 \end{pmatrix} \tag{A.24}$$

If an element (such as element 23 or 27 in Fig. A.2) contains a crack tip, it will be partially cut by the crack surface, and needs to be enriched by asymptotic crack-tip functions of the form:

$$F(r,\theta) = \{\sqrt{r}sin\left(\frac{\theta}{2}\right), \sqrt{r}cos\left(\frac{\theta}{2}\right), \sqrt{r}sin\left(\frac{\theta}{2}\right)sin\theta, \sqrt{r}cos\left(\frac{\theta}{2}\right)sin\theta\} \tag{A.25}$$

As shown in Fig. A.2, the elements in the domain can be classified as enriched elements if they are cut through (partially or completely) by a crack. Elements that share one or more nodes with an enriched element are classified as blending elements, while those that do not share any nodes with enriched elements are classified as standard elements. Furthermore, nodes that bound enriched elements are referred to as enriched nodes (and can either be crack-tip enriched or Heaviside nodes) whereas those that bound standard elements are referred to as standard nodes.

References

Batchelor, G., 1967. An Introduction to Fluid Dynamics. Cambridge University Press.

Biot, M.A., 1941. General theory of three-dimensional consolidation. J. Appl. Phys. 12 (2), 155–164, Publisher: American Institute of Physics.

Bostrøm, B., Skomedal, E., 2004. Reservoir geomechanics with ABAQUS. In: 2004 ABAQUS Users' Conference. pp. 117–131.

Chukwudozie, C., 2016. Application of the Variational Fracture Model to Hydraulic Fracturing in Poroelastic Media. (Ph.D. thesis). Louisiana State University, Baton Rouge.

Clifton, R.J., Abou-Sayed, A.S., 1981. A variational approach to the prediction of the three-dimensional geometry of hydraulic fractures. In: SPE/DOE Low Permeability Gas Reservoirs Symposium. Society of Petroleum Engineers.

Coussy, O., 2007. Revisiting the constitutive equations of unsaturated porous solids using a Lagrangian saturation concept. Int. J. Numer. Anal. Methods Geomech. 31 (15), 1675–1694, Publisher: Wiley Online Library.

Ţene, M., Bosma, S.B., Al Kobaisi, M.S., Hajibeygi, H., 2017. Projection-based embedded discrete fracture model (pEDFM). Adv. Water Resour. 105, 205–216, Publisher: Elsevier.

Dolbow, J.E., 1999. An Extended Finite Element Method with Discontinuous Enrichment for Applied Mechanics. Northwestern university.

Dontsov, E., Peirce, A., 2015. An enhanced pseudo-3D model for hydraulic fracturing accounting for viscous height growth, non-local elasticity, and lateral toughness. Eng. Fract. Mech. 142, 116–139.

Duarte, C.A., Oden, J.T., 1996. H-p clouds—An h-p meshless method. Numer. Methods Partial Differential Equations: Int. J. 12 (6), 673–705, Publisher: Wiley Online Library.

Efendiev, Y., Lee, S., Li, G., Yao, J., Zhang, N., 2015. Hierarchical multiscale modeling for flows in fractured media using generalized multiscale finite element method. GEM-Int. J. Geomath. 6 (2), 141–162, Publisher: Springer.

Geertsma, J., De Klerk, F., 1969. A rapid method of predicting width and extent of hydraulically induced fractures. J. Pet. Technol. 21 (12), 1–571, Publisher: Society of Petroleum Engineers.

Janssen, M., Zuidema, J., Wanhill, R., 2006. Fracture Mechanics VSSD. Delft.

Jiang, J., Younis, R.M., 2017. An improved projection-based embedded discrete fracture model (pEDFM) for multiphase flow in fractured reservoirs. Adv. Water Resour. 109, 267–289. http://dx.doi.org/10.1016/j.advwatres.2017.09.017, Publisher: Elsevier Ltd.

Karimi-Fard, M., Firoozabadi, A., 2001. Numerical simulation of water injection in 2D fractured media using discrete-fracture model. In: SPE Annual Technical Conference and Exhibition. Society of Petroleum Engineers, New Orleans, Louisiana, USA, http://dx.doi.org/10.2118/71615-MS.

Khoei, A.R., 2014. Extended Finite Element Method: Theory and Applications. John Wiley & Sons.

Khristianovic, S., Zheltov, Y.P., 1955. Formation of vertical fractures by means of highly viscous liquid. In: World Petroleum Congress Proceedings. pp. 579–586.

Kim, J., 2010. Sequential Methods for Coupled Geomechanics and Multiphase Flow, Vol. 71. Citeseer.

Kim, J.-G., Deo, M.D., 2000. Finite element, discrete-fracture model for multiphase flow in porous media. AIChE J. 46 (6), 1120–1130. http://dx.doi.org/10.1002/aic.690460604, Publisher: Wiley Subscription Services, Inc., A Wiley Company.

Li, Q., Fei, W., Ma, J., Jing, M., Wei, X., 2019. Coupled CO2 sequestration simulation using ABAQUS and ECLIPSE. Environ. Geotech. 1–12, Publisher: Thomas Telford Ltd.

Li, L., Lee, S.H., 2008. Efficient field-scale simulation of black oil in a naturally fractured reservoir through discrete fracture networks and homogenized media. SPE Reserv. Eval. Eng. 11 (04), 750–758, Publisher: Society of Petroleum Engineers.

Lie, K.A., 2019. An Introduction To Reservoir Simulation using MATLAB/GNU Octave: User Guide for the MATLAB Reservoir Simulation Toolbox (MRST). Cambridge University Press, Cambridge.

Liu, Z., Chen, M., Zhang, G., 2014. Analysis of the influence of a natural fracture network on hydraulic fracture propagation in carbonate formations. Rock Mech. Rock Eng. 47 (2), 575–587.

Mandel, J., 1953. Consolidation des sols (étude mathématique). Geotechnique 3 (7), 287–299, Publisher: Thomas Telford Ltd.

Melenk, J.M., Babuška, I., 1996. The partition of unity finite element method: basic theory and applications. In: Research Report/Seminar Für Angewandte Mathematik, Vol. 1996. Eidgenössische Technische Hochschule, Seminar für Angewandte Mathematik, Issue: 01.

Moës, N., Dolbow, J., Belytschko, T., 1999. A finite element method for crack growth without remeshing. Internat. J. Numer. Methods Engrg. 46 (1), 131–150, Publisher: Wiley Online Library.

Moinfar, A., Varavei, A., Sepehrnoori, K., Johns, R.T., 2013. Development of a coupled dual continuum and discrete fracture model for the simulation of unconventional reservoirs. In: SPE Reservoir Simulation Symposium. Society of Petroleum Engineers.

Nolte, K.G., 1979. Determination of fracture parameters from fracturing pressure decline. In: SPE Annual Technical Conference and Exhibition. OnePetro.

Nolte, K., Maniere, J., Owens, K., 1997. After-closure analysis of fracture calibration tests. In: SPE Annual Technical Conference and Exhibition. OnePetro.

Olorode, O., Wang, B., Rashid, H.U., 2020. Three-dimensional projection-based embedded discrete-fracture model for compositional simulation of fractured reservoirs. SPE J. Publisher: Society of Petroleum Engineers.

Perkins, T., Kern, L.R., 1961. Widths of hydraulic fractures. J. Pet. Technol. 13 (09), 937–949, Publisher: Society of Petroleum Engineers.

Rahman, M., Rahman, S., 2013. Studies of hydraulic fracture-propagation behavior in presence of natural fractures: Fully coupled fractured-reservoir modeling in poroelastic environments. Int. J. Geomech. 13 (6), 809–826.

Ren, G., Younis, R.M., 2020. An integrated numerical model for coupled poro-hydro-mechanics and fracture propagation using embedded meshes. arXiv preprint arXiv:2008.03186.

Rice, J.R., 1968. A path independent integral and the approximate analysis of strain concentration by notches and cracks. J. Appl. Mech. 35 (2), 379–386. http://dx.doi.org/10.1115/1.3601206, arXiv:https://asmedigitalcollection.asme.org/appliedmechanics/article-pdf/35/2/379/5449160/379_1.pdf.

Siebrits, E., Peirce, A.P., 2002. An efficient multi-layer planar 3D fracture growth algorithm using a fixed mesh approach. Internat. J. Numer. Methods Engrg. 53 (3), 691–717.

Sneddon, I., Lowengrub, M., 1969. Crack Problems in the Classical Theory of Elasticity, Vol. 29. John Willey & Sons, New York.

Soliman, M.Y., Craig, D.P., Bartko, K.M., Rahim, Z., Adams, D.M., 2005. Post-closure analysis to determine formation permeability, reservoir pressure, residual fracture properties. In: SPE Middle East Oil and Gas Show and Conference. OnePetro.

Terzaghi, K., Peck, R.B., Mesri, G., 1996. Soil Mechanics in Engineering Practice. John Wiley & Sons.

Verruijt, A., 2013. Theory and problems of poroelasticity. Delft Univ. Technol. 71.

Wang, C., Huang, Z., Wu, Y.-S., 2020. Coupled numerical approach combining X-FEM and the embedded discrete fracture method for the fluid-driven fracture propagation process in porous media. Int. J. Rock Mech. Min. Sci. 130, 104315, Publisher: Elsevier.

Yoda, M., 1980. The J-integral fracture toughness for mode II. Int. J. Fract. 16 (4), R175–R178. http://dx.doi.org/10.1007/BF00018247.

Zeng, Q., Liu, Z., Wang, T., Gao, Y., Zhuang, Z., 2018. Fully coupled simulation of multiple hydraulic fractures to propagate simultaneously from a perforated horizontal wellbore. Comput. Mech. 61 (1), 137–155, ISBN: 1432-0924 Publisher: Springer.

Zoback, M.D., 2010. Reservoir Geomechanics. Cambridge University Press.